Chemical Science

ROYAL SOCIETY OF CHEMISTRY

REVIEW

View Article Online
View Journal

Cite this: DOI: 10.1039/d5sc04478b

Layer-by-layer assembly: an emerging, tailored and robust platform for solar water splitting

Wen-Cheng Liu,†[a] Yan-Qing Cai†[c] and Fang-Xing Xiao *[ab]

Photoelectrochemical (PEC) water splitting represents a highly promising technology to convert solar energy into clean and renewable chemical fuels. Among the various strategies utilized for customizing photoelectrodes, layer-by-layer (LbL) assembly has emerged as a green, simple, and easily accessible technique for rationally constructing multilayered heterostructures in terms of versatility, flexibility, and atomic-level interface configuration modulation. However, precise design of robust photoelectrodes based on LbL assembly still remains in the exploratory stage. This review comprehensively summarizes the recent advancements in the fabrication of composite multilayer photoanodes *via* LbL assembly, highlighting the LbL assembly construction with diverse substrates (*e.g.*, metal oxides, transition metal sulfides) and building blocks of varying sizes and dimensions (*e.g.*, quantum dots, nanoclusters, nanoparticles, nanosheets). Furthermore, this review underscores the role of these building blocks in extending the light absorption and improving the solar water oxidation performance. Most importantly, the latest endeavors devoted to mediating directional charge transfer routes in artificial PEC systems are specifically summarized. Finally, prospects and challenges of LbL assembly technology in photoelectrode engineering for PEC water splitting are outlined, aiming to inspire innovative strategies for the smart design of composite nanostructured photoelectrodes towards solar energy conversion.

Received 18th June 2025
Accepted 28th August 2025

DOI: 10.1039/d5sc04478b

rsc.li/chemical-science

1. Introduction

In recent decades, the technology of converting water into green hydrogen fuel using abundant, green, and sustainable solar energy has become a crucial solution to address the fossil fuel depletion crisis.[1] Currently, the predominant solar-driven water-splitting methods include photocatalysis, photothermal catalysis, and photoelectrochemical (PEC) catalysis. However, photocatalytic hydrogen production is hindered by rapid charge recombination (<1 ns), low solar-to-hydrogen (STH) efficiency (<3%), and poor long-term stability.[2] Photothermal catalysis consumes a large amount of additional energy. In contrast, a PEC cell leverages the photo-electron coupling mechanism to achieve STH conversion efficiencies exceeding 10% (*e.g.*, copper indium gallium selenide and halide perovskite-based cells), signifying its emerging potential for industrial-scale hydrogen production.[3] Compared with heterogeneous photocatalysis, PEC technology can employ a broader scope of interface engineering optimization strategies to enhance the charge separation and corrosion resistance of photoelectrodes, thereby improving the stability of hydrogen evolution. Moreover, PEC cells generally operate under mild conditions, significantly reducing the emission of harmful byproducts and providing a more cost-effective solution for solar-driven hydrogen production.[4] Consequently, PEC water splitting has emerged as a key technology for solar-to-hydrogen conversion in the pursuit of sustainable energy solutions.

In order to improve the STH conversion efficiency of PEC systems, previous endeavors have been mainly devoted to doping with impurity atoms or ions, surface passivation and modification, and designing Type-II or Z-scheme heterojunctions.[5] Although these methods can improve the efficiency of photoelectrocatalysis to some extent, current research frontiers are mainly centered on exploring new composite photoelectrodes, but have met with limited success. The emergence of nanotechnology provides a feasible and effective way to readily construct high-efficiency composite artificial photosystems.[6] Currently, bottom-up thin film fabrication methods primarily include Langmuir–Blodgett (LB), self-assembled monolayers (SAMs), chemical vapor deposition (CVD), hydrothermal techniques, and electrodeposition,[7] but they inevitably encounter obstacles in practical applications. For example, the LB method typically requires semiconductor substrates with high mechanical strength. The SAM method faces issues of insufficient stability and a complex molecular design process when preparing a multilayer structure. The CVD method incurs high production costs in the actual fabrication of thin films and generates toxic byproducts that are harmful to the

[a]College of Materials Science and Engineering, Fuzhou University, New Campus, Minhou, Fujian Province, 350108, China. E-mail: fxxiao@fzu.edu.cn
[b]State Key Laboratory of Structural Chemistry, Fujian Institute of Research on the Structure of Matter, Chinese Academy of Sciences, Fuzhou, Fujian 350002, PR China
[c]School of Advanced Manufacturing, Fuzhou University, Jinjiang, 362200, PR China
† These two authors contributed equally to this work.

environment.[8] Therefore, there is an urgent need to develop precise, efficient, and cost-effective thin film fabrication methods to integrate nanoscale building blocks with semiconductors for crafting novel composite photoelectrodes.

Thus far, the layer-by-layer (LbL) assembly approach has been developed to address the limitations of conventional bottom-up thin-film fabrication techniques. It is suitable for the composite assembly of a wide range of materials, including polyelectrolytes, nanoparticles, biomacromolecules, and organic small molecules, and facilitates the preparation of both organic and inorganic thin films.[9] In addition, LbL assembly provides tunable multilayer nanoarchitectures, enabling precise control of key parameters such as film thickness, morphology, and properties at the nanoscale, with the preparation process being environmentally friendly and cost-efficient. Furthermore, LbL assembly improves the stability of composite nanomaterials through orderly interface design *via* molecular interactions such as electrostatic adsorption and covalent cross-linking.[10] Consequently, LbL assembly provides a versatile platform for fabricating novel heterostructured photoelectrodes for solar energy conversion. Although some reviews have summarized the progress in the fabrication of spatially multilayered architectures *via* LbL assembly, they lack a systematic and insightful elaboration on the correlation between the structure of building blocks and PEC water splitting performances. Furthermore, charge transport characteristics mediated by the unique interface configuration endowed by LbL assembly have not yet been elucidated.

Motivated by these considerations, the current review aims to provide a detailed overview of the up-to-date advancements in PEC water splitting systems constructed by LbL assembly under ambient conditions. This review initially elucidates the essential principles of LbL assembly and PEC water splitting, followed by a comprehensive discussion of heterostructured photoelectrodes assembled with diverse types of substrates (*e.g.*, metal oxides, transition metal sulfides, *etc.*) and functional building blocks of various sizes and dimensions (*e.g.*, quantum dots, nanoclusters, nanoparticles, nanosheets, *etc.*). In addition, the present review summarizes the mechanistic correlation between the spatially hierarchical structures of multilayered photoelectrodes and their PEC water splitting performances. This work provides valuable information on the exploration of a large variety of LbL-assembled PEC systems with fine tuning of charge transport and separation for solar-to-hydrogen conversion.

2. A brief overview of LbL assembly

Layer-by-layer (LbL) assembly represents a nanoscale fabrication technique that exploits complementary interactions, such as electrostatic force and hydrogen bonding, to sequentially deposit materials onto interfaces with high precision.[11] The concept of LbL assembly was first introduced in 1966 by Iler *et al.*, who systematically studied the adsorption behavior of small particles, multivalent ions, and water-soluble polymers, laying the foundation for its interfacial mechanism.[12] A major milestone in LbL assembly came in 1991 with the work of Decher and colleagues, who successfully fabricated and systematically characterized 100-layer polyelectrolyte films.[13] This pioneering work established LbL assembly as a robust and adaptable platform for fabricating nanostructured thin films with diverse functional applications. Building on its core principle of integrating multiple functional building blocks, LbL assembly offers precise control over critical parameters, including film thickness, composition, and architecture, thereby enabling the rational design of spatially organized multilayered nanostructures on a wide range of substrates.[14] Compared with conventional thin film fabrication techniques, LbL assembly provides superior precision, enhanced stability, and improved fabrication efficiency, addressing limitations such as poor interfacial control and material compatibility. These unique advantages have enabled LbL assembly to be widely adopted in various disciplines, including energy storage (*e.g.*, supercapacitors and lithium-ion batteries), catalysis, biomedical drug delivery, electronics, and photonic devices.[7a]

In order to adapt to the assembly of building blocks with different geometric shapes and specific functional requirements, LbL assembly technology has developed assembly modes such as immersion assembly, spin assembly, spray assembly, fluidic assembly and electromagnetic assembly (Fig. 1a).[15] Among these methods, spray assembly or spin assembly is generally applicable to planar substrates and requires complex equipment (*e.g.*, high-pressure spray guns or centrifuges).[10] In contrast, immersion assembly, performed within the solution phase, exhibits broad adaptability to substrates with diverse geometric characteristics, including porous structures, curved surfaces, and three-dimensional (3D) architectures. This method promotes the uniform deposition of functional building blocks, thereby offering advantages for the fabrication of structurally complex PEC devices. Furthermore, unlike fluidic assembly, which requires stringent control of hydrodynamic conditions, and electromagnetic assembly, which is limited to magnetically responsive materials,[16] immersion assembly enables the formation of stable multilayer structures without the need for elaborate assembly protocols.[17] Therefore, immersion assembly represents the most versatile approach for LbL assembly of photoelectrodes, owing to its broad material compatibility, operational simplicity, and precise controllability.

Beyond the different assembly techniques, the molecular interactions underlying the LbL assembly process include electrostatic interaction, hydrogen bonding interaction, covalent bonding interaction, host–guest interaction, and coordination chemistry interaction.[18] Notably, electrostatic interaction represents the predominant driving force in LbL assembly, owing to its wide applicability, straightforward processing, and excellent interface stability.[19] As illustrated in Fig. 1b, the initial step of electrostatically driven immersion LbL assembly involves immersing a positively charged substrate in an anionic building block solution containing functional substances, such as polymers or nanoparticles. This process results in the formation of a single-layer film on the substrate surface. Following each adsorption step, the substrate is thoroughly rinsed with ultrapure water to eliminate physically

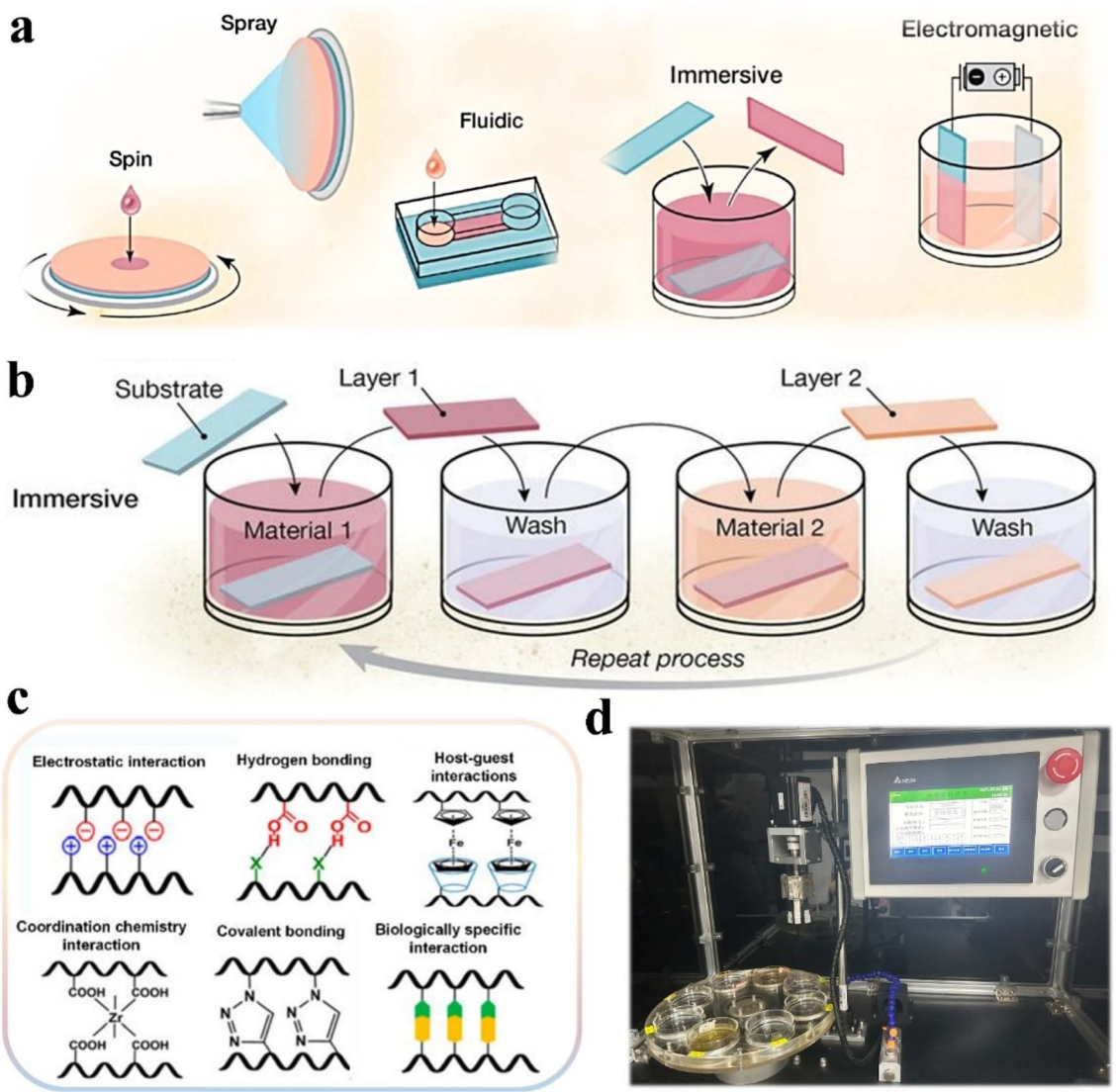

Fig. 1 (a) LbL assembly techniques for different assembly modes (reprinted with permission from ref. 16, Copyright 2016 American Chemical Society). (b) Schematic illustration of the immersion LbL assembly process (reprinted with permission from ref. 10, Copyright 2015, American Association for the Advancement of Science). (c) Molecular interactions between functional building blocks in LbL assembly (reprinted with permission from ref. 26, Copyright 2018 Multidisciplinary Digital Publishing Institute). (d) Actual photograph of the automated LbL assembly equipment designed by our group, used for LbL assembly of spatially multilayered heterostructure photoelectrodes.

adsorbed substances while preserving the chemically bonded monolayer. Subsequently, the single-layer film is immersed in a cationic solution, facilitating the formation of a double-layer film structure through charge attraction.[20] By repeating this cycle, a desired n-layer film structure can be achieved, allowing for precise control of composition and concentration at the nanoscale by adjusting the number of layers.[21]

In addition to the core electrostatic interaction mechanism, the key parameters regulating the LbL assembly process such as the charge density of the polyelectrolyte (PE), reaction temperature, pH value, ionic strength, and adsorption time are essential in determining the thickness, internal structure, and stability of the multilayer film.[22] Importantly, precise adjustment of these parameters to optimize interfacial connection between the different building blocks remains an area of ongoing investigation. Establishing standardized and systematic assembly schemes is critical for enhancing the structural robustness and functional efficiency of LbL-assembled architectures. For example, in the MOs/(PDDA/Au_x NCs)$_n$ multilayer heterostructure photoanodes with efficient cascade charge transfer characteristic, the oppositely charged PDDA and Au_x NCs serve as building blocks for LbL assembly construction.[23] It is essential to precisely adjust the concentration of building blocks and assembly cycle, as excessive polyelectrolyte and functional building block deposition can both lead to adverse effects. In addition, the assembly sequence between different building blocks is also crucial, as it is closely related to fine-tuning of electron transfer in the multilayer structure. For

example, as demonstrated by Li *et al.*, multilayer photoanodes prepared with different assembly sequences of PDDA and MXene quantum dots show significantly different photocurrent densities, implying that the cascade charge transfer pathway can be rationally designed *via* structure modulation.[24] In general, the rational design of the LbL-assembled multilayer heterostructure needs to consider the following key points: (1) band alignment between building blocks and semiconductor materials such as Type-II and Z-scheme band structure, (2) the roles played by polyelectrolytes between building blocks such as promoting charge transfer, serving as molecular glue, and forming an interfacial dipole, and (3) stability of the connection between functional building blocks. The LbL assembly principle based on molecular interaction has been widely accepted and will provide inspiring guidance for the future design and optimization of LbL-assembled multilayer photoelectrodes.

As shown in Fig. 1d, our group has independently developed an automated LbL assembly device for fabrication of spatially multilayered heterostructure photoelectrodes. This equipment effectively addresses the issues of low efficiency, non-uniform coating, and poor quality in the traditional manual LbL process, demonstrating high automation levels with superior coating uniformity and quality. Specifically, the device enables precise control of critical parameters including assembly sequence, coating duration, deposition rate, and cycle number through an intelligent control system, significantly reducing manual operation time while overcoming the technical limitations of conventional methods in terms of efficiency and uniformity. Furthermore, the integrated N_2 atmosphere protection and temperature control modules substantially enhance coating quality and film stability, offering considerable practical value. Notably, this LbL assembly system exhibits distinct advantages over conventional multilayer fabrication techniques such as CVD, electrodeposition, hydrothermal, LB, and SAM methods. Specifically, our LbL device operates even under ambient conditions with minimal material consumption (90% utilization rate) and broad compatibility with diverse inorganic or organic materials, demonstrating remarkable advantages in operational simplicity, safety, and cost-effectiveness.[25] Consequently, leveraging our team's proprietary high-precision automated control system, LbL assembly technology is poised to overcome traditional process limitations, enabling efficient and stable large-scale production while providing robust technical support for industrial manufacturing of next-generation functional composite photoelectrodes.

3. Principle of PEC water splitting

PEC water splitting, which utilizes semiconductor materials to absorb solar energy and drive the redox reactions of water enabling the sustainable production of hydrogen, is regarded as a crucial strategy to alleviate the global energy crisis.[27] The origins of PEC water splitting can be traced back to A. E. Becquerel's pioneering work in 1839, when he first observed the photocurrent in silver halide materials.[28] This foundational discovery laid the groundwork for subsequent advancements in solar energy conversion. However, the true breakthrough in integrating PEC systems into solar energy conversion was propelled by the seminal contributions of Fujishima and Honda.[29] As illustrated in Fig. 2a–c, the fundamental principle of PEC water splitting involves photoinduced redox reactions at semiconductor electrodes under light irradiation, resulting in the production of hydrogen (H_2) and oxygen (O_2).[30] PEC reactions usually occur in electrochemical cells; in a typical PEC system, an electron-rich n-type semiconductor photoanode (*e.g.*, TiO_2, Fe_2O_3, or $BiVO_4$) absorbs incident photons, exciting electrons from the valence band (VB) to the conduction band (CB), thereby generating electron–hole pairs. The photogenerated electrons migrate through an external circuit to the hole-rich p-type semiconductor (*e.g.*, Cu_2O, NiO, or CoO), where they reduce protons (H^+) to H_2. Simultaneously, the holes accumulated in the VB oxidize water molecules at the photoanode, releasing O_2.[31] Nevertheless, the rapid recombination of photogenerated electron–hole pairs critically impedes charge separation, representing a major barrier to achieving high-efficiency PEC water splitting. To address this issue, an external bias is typically applied in PEC systems to facilitate charge separation and effectively overcome the inherent energy barrier of semiconductors. Furthermore, co-catalysts (*e.g.*, Pt, graphene, NiFe-layered double hydroxides) can be introduced in the fabrication of photoelectrodes to reduce the overpotential and enhance the reaction kinetics.[32] By synergistically enhancing light absorption, facilitating charge separation, and optimizing surface catalytic activity, PEC water splitting enables highly efficient solar-to-hydrogen energy conversion. This technology provides a promising pathway for solar-driven hydrogen production, offering a critical solution to the efficient storage and utilization of renewable energy.

Specifically, the chemical reactions of hydrogen evolution reaction (HER) and oxygen evolution reaction (OER) involved in the PEC water splitting reaction are as follows:

Reaction at the anode:

$$2H_2O + 4h^+ \rightarrow O_2 + 4H^+ \quad (1)$$

Reaction at the cathode:

$$4H^+ + 4e^- \rightarrow 2H_2 \quad (2)$$

Net Reaction:

$$2H_2O \rightarrow 2H_2 + O_2 \quad (3)$$

To comprehensively evaluate PEC system performance, several critical efficiency metrics are utilized. These metrics include the standard solar-to-hydrogen conversion efficiency (η_{STH}), applied bias photon-to-current efficiency (ABPE), incident photon-to-current conversion efficiency (IPCE), charge transfer lifetime (τ), faradaic efficiency (FE), stability, and electrochemical active surface area (ECSA).[34] Each parameter provides distinct insights into the catalytic characteristics of PEC systems. Among these indicators, η_{STH} represents the ultimate performance metric for all solar conversion photosystems. The η_{STH} is quantitatively defined as the ratio between the

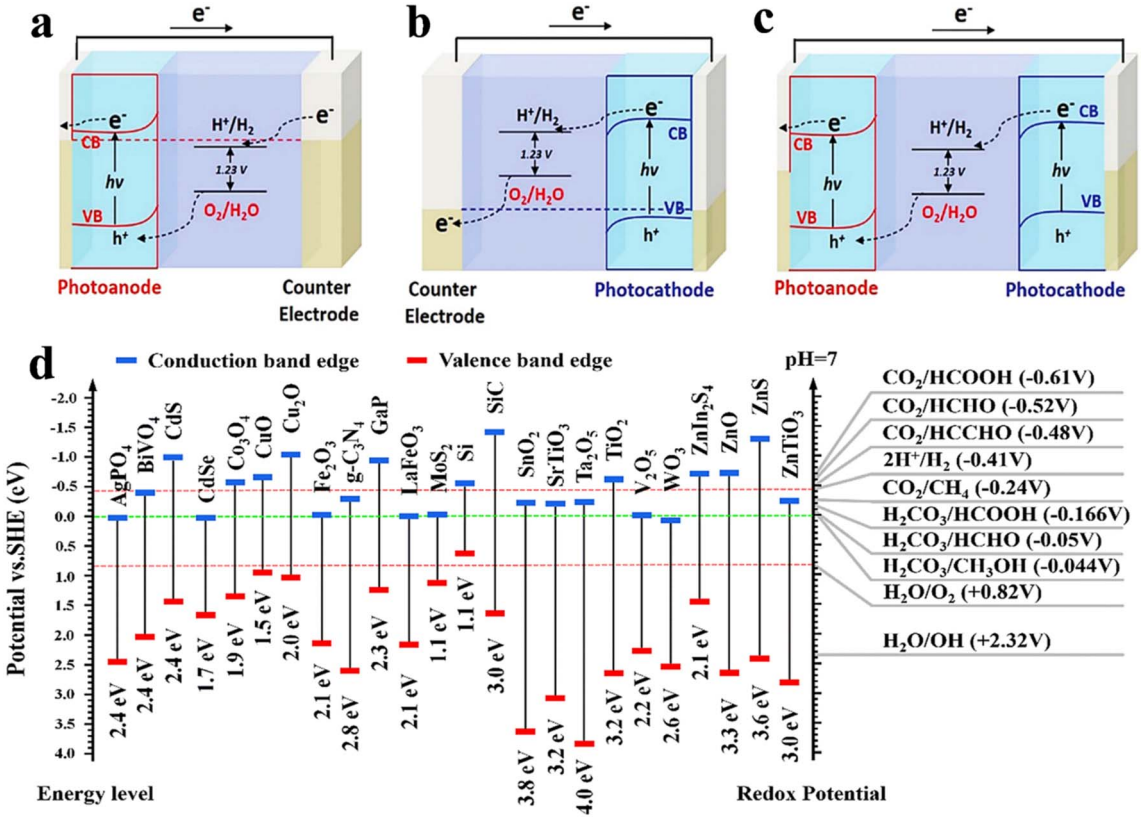

Fig. 2 Schematic illustration of PEC water splitting using (a) a photoanode, (b) photocathode, and (c) a tandem configuration combining both a photoanode and photocathode (reprinted with permission from ref. 30, Copyright 2014 Wiley-VCH Verlag). (d) CB and VB edges of semiconductor photocatalysts, along with their corresponding redox potentials in aqueous media (reprinted with permission from ref. 33, Copyright 2024 Royal Society of Chemistry).

energy content of evolved hydrogen (calculated *via* Gibbs free energy $\Delta G = 237$ kJ mol^{-1}) and the incident solar energy input:[35]

$$\eta_{STH} = \frac{\text{Total energy generated}}{\text{Total energy input}} = \frac{\Delta G \times r_{H_2}}{P_{sun} \times S} \quad (4)$$

where r_{H_2} denotes the hydrogen evolution rate (mol s^{-1}), P_{sun} represents the incident light intensity (100 mW cm^{-2} under AM 1.5G illumination), and S is the illuminated area of the photoelectrode (cm^2).

In PEC photosystems, ABPE is essential for quantifying the STH conversion efficiency under applied bias conditions. It quantifies the efficiency with which absorbed solar photons generate photocurrent at a specified applied bias. The ABPE is calculated using the following equation:[36]

$$\eta = \frac{I_{ph}(1.23 - |V|)}{P_{light}} \quad (5)$$

where I_{ph} represents the photocurrent density (mA cm^{-2}) at the measured potential, V denotes the applied bias *versus* the reversible hydrogen electrode (RHE), and P_{light} is the light intensity. Under monochromatic light irradiation, IPCE quantifies the number of charge carriers generated per incident photon reaching the photoelectrode surface:[37]

$$\text{IPCE(at } \lambda) = \frac{-J_{PEC} \times 1240}{\lambda \times P_{mono}} \times 100\% \quad (6)$$

where J_{PEC} denotes the photocurrent (mA cm^{-2}) and P_{mono} (mW cm^{-2}) is the optical density at the optical wavelength λ (nm). Charge transfer lifetime (τ) at the semiconductor–electrolyte interface is also critical for assessing PEC cell performance. It is typically determined from electrochemical impedance spectroscopy (EIS) measurements at the photoelectrode–electrolyte interface, expressed as:

$$\tau = \frac{1}{2\pi f_{peak}} \quad (7)$$

where f_{peak} represents the peak frequency observed in the Bode phase spectrum obtained from EIS measurements. Faradaic efficiency (FE, η_F) quantifies the catalytic selectivity by exploring the ratio of the actual gas produced to the theoretical yield predicted from the photocurrent. This parameter reflects the energy conversion efficiency of the PEC system and is defined as follows:[35]

$$FE_{O_2} = \frac{Y_{O_2}}{J_{photo} \times A \times \frac{T}{4eN_A}} \times 100\% \quad (8)$$

$$FE_{H_2} = \frac{Y_{H_2}}{J_{photo} \times A \times \frac{T}{2eN_A}} \times 100\% \quad (9)$$

where Y represents the experimentally measured amount of oxygen or hydrogen gas (mol), A is the effective illuminated area (cm^2) of the electrode, e is the elementary charge (C), T is the reaction duration (s), and the Avogadro constant $N_A = 6.02 \times 10^{23}$ mol^{-1}.

Electrochemical active surface area (ECSA) refers to the actual surface area of electrode materials that participates in electrochemical reactions, reflecting effective catalyst utilization. Unlike geometric area, ECSA considers microstructural features such as surface roughness, porosity, and degree of active site exposure, making it a critical parameter for evaluating photoelectrode performance. The electrochemical double-layer capacitance (C_{dl}) at catalyst surfaces is typically determined by measuring non-faradaic capacitive currents from cyclic voltammetry curves at multiple scan rates. The ECSA calculation formula is as follows:[38]

$$ECSA = \frac{C_{dl}}{C_s} \quad (10)$$

where C_{dl} is the double-layer capacitance of the electrode and C_s is the specific capacitance of the standard smooth electrode (μF cm^{-2}).

Efficient PEC water splitting holds potential to economically compete with conventional fossil fuel-based hydrogen production technologies, provided that its STH conversion efficiency approaches or exceeds approximately 10% (comparable to an efficiency threshold dictated by fossil fuel economics).[39] The energy band structure of semiconductor materials primarily determines the achievable efficiency of PEC water splitting. For spontaneous PEC water splitting without an external bias, the semiconductor must have a minimum bandgap energy exceeding the thermodynamic requirement of 1.23 eV, corresponding to the Gibbs free energy for water splitting.[40] Furthermore, the CB edge must lie at a more negative potential, and the VB edge must be more positive, relative to the hydrogen evolution (0 V *vs.* RHE) and oxygen evolution potentials (1.23 V *vs.* RHE), respectively. Fig. 2d summarizes the CB and VB positions of representative semiconductor photocatalysts, which are essential for rational adjustment and optimization of the energy-level structures of catalyst in designing photoelectrodes.[41] A catalyst with a bandgap of 1.6–2.4 eV is generally considered optimal as it can maximize the absorption of sunlight while overcoming the overpotential in charge transfer between the photoanode and photocathode and minimizing energy loss. Beyond band structure considerations, PEC water splitting efficiency significantly depends on the interfacial charge transfer kinetics at the semiconductor–electrolyte interface. Achieving efficient charge separation and transport is essential for suppressing charge recombination and maximizing the overall photocurrent generation efficiency.[42] Consequently, designing high-performance PEC systems necessitates a coordinated approach that integrates semiconductor band engineering with optimization strategies for enhancing charge separation, to enable efficient solar energy conversion.

4. Novel LbL-assembled photoelectrodes for PEC water splitting

In this section, we introduce the design and application of novel LbL-assembled heterostructures for PEC water splitting, focusing particularly on employing various substrate materials and assembling functional building blocks. We first categorize various semiconductors, including TiO_2, WO_3, ZnO, $BiVO_4$, and CdS, as substrates for LbL assembly, leveraging their unique light absorption properties and energy band structures to enhance solar water oxidation efficiency. Additionally, we elucidate the rational integration of quantum dots (QDs) (*e.g.*, transition metal chalcogenide QDs, graphene QDs, and MXene QDs), nanoclusters (NCs) (*e.g.*, metal NCs and polyoxometalate NCs), and nanoparticles (NPs) (*e.g.*, metal NPs and up-conversion NPs) as functional building blocks. These components exhibit a remarkable ability to promote charge separation or extend light absorption, which are the key factors in improving PEC performances. Furthermore, we investigate the LbL assembly of composite multilayer films utilizing graphene nanosheets and polyelectrolyte multilayers as the building blocks, where the constructed high-efficiency charge transfer pathways effectively enhance the PEC efficiency of photoelectrodes. By summarizing these assembly strategies, this section will elucidate the structure–performance relationship of spatially multilayered photoelectrodes fabricated by the LbL assembly technique.

4.1. LbL assembly with different semiconductors as substrates

4.1.1. TiO_2. Titanium dioxide (TiO_2) is one of the most widely studied materials in PEC systems due to its favorable bandgap (3.0–3.2 eV), excellent charge mobility, stable physicochemical properties, and economical feasibility.[43] To improve the solar energy conversion efficiency, various TiO_2 photoelectrodes with different sizes and morphologies have been developed, including zero-dimensional (0D) NPs, one-dimensional (1D) nanorods and nanotubes, and two-dimensional (2D) nanosheets.[44] Among them, 0D NPs face limitations in mediating the charge transport pathway, while 2D nanosheet materials involve a complicated synthesis process and easily fall off during the LbL assembly process.[45] In contrast, 1D TiO_2 structures such as nanorod arrays and nanotube arrays offer efficient photogenerated charge transport along the axial direction, coupled with simple fabrication processes and structural stability, making them the preferred choice for construction of TiO_2-based LbL-assembled photoelectrodes. For example, Yang *et al.* employed the LbL assembly technique to load a p-type porphyrin-based metal–organic framework (MOF) onto TiO_2 nanorod arrays (TNRAs), resulting in multilayer p–n heterojunction photoanodes.[46] The TNRAs and MOF coating are connected through coordination bond

interaction. Importantly, the built-in electric field of the p–n heterojunction effectively facilitates the charge transfer from TiO_2 to the MOF. Furthermore, the unique porous structure of the MOF enhances the charge injection and separation efficiency at the photoanode/electrolyte interface. In another work on TNRAs, Tang *et al.* loaded poly (dimethyl diallyl ammonium chloride) (PDDA) and Ag_x NCs onto the TNRA substrate *via* LbL assembly to obtain spatially multilayered photoanodes (Fig. 3a and b).[47] Specifically, PDDA carries an intrinsic positive charge, while Ag_x NCs, encapsulated by L-glutathione (GSH) ligands, exhibit negative charge characteristics, enabling their integration *via* electrostatic interactions. The zeta potential measurements effectively confirmed this mechanism, with the TNRAs/PDDA potential being +6.04 mV and the Ag_x NC potential being −7.08 mV. As shown in Fig. 3c, compared with the pristine TNRAs, the TNRAs/(PDDA/Ag_x NCs)$_4$ multilayer photoanode demonstrates the highest photocurrent density (40 μA cm^{-2}) under visible light illumination. Moreover, when the assembly sequence of PDDA and Ag_x NCs was altered, the resulting multilayer heterostructures demonstrated significantly lower photocurrent density compared with TNRAs/(PDDA/Ag_x NCs)$_4$. These results strongly indicate that the rationally designed multilayer heterostructure is crucial for significantly enhancing the PEC water oxidation efficiency of composite photoanodes. To further explore the universality of Ag NCs, Tang *et al.* constructed similar PEC systems using Ag_9 NCs, Ag_{16} NCs, and Ag_{31} NCs as the building blocks (Fig. 3d). The results consistently show that the LbL-assembled TNRAs/(PDDA/Ag NCs)$_4$ multilayer photoanodes exhibited the optimal solar energy conversion efficiency. Considering that the band structures of these Ag NCs are aligned with the energy level of the wide-bandgap semiconductor TiO_2, and that the LbL assembly technique ensures tight and stable heterointerfaces between different building blocks, a theoretical model of such well-structured

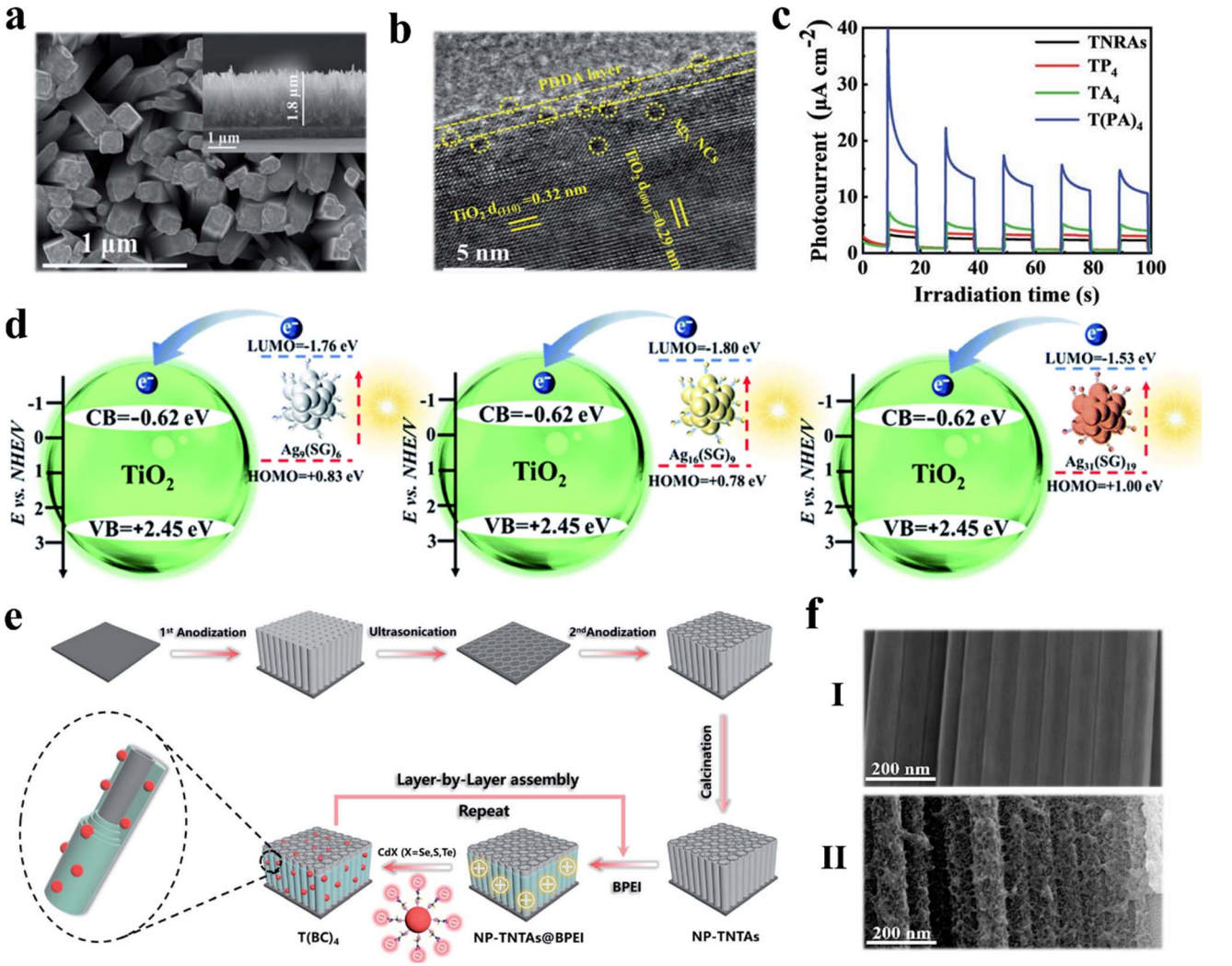

Fig. 3 (a) Top-view scanning electron microscopy (SEM) images, (b) high-resolution transmission electron microscopy (HR-TEM) images, and (c) transient photocurrent (*I*–*t*) responses of TNRAs/(PDDA/Ag_x NCs)$_4$ multilayer heterostructures. (d) Schematic representation of the energy band structure of TNRA and Ag NCs [Ag_9 (SG)$_6$NCs, Ag_{16} (SG)$_9$NCs, Ag_{31} (SG)$_{19}$NCs] (reprinted with permission from ref. 47, Copyright 2022 Royal Society of Chemistry). (e) Schematic illustration for LbL assembly of TNTA/(BPEI/CdSe QDs)$_4$ photoanodes. (f) Cross-sectional SEM images of (I) TNTAs and (II) TNTA/(BPEI/CdSe QDs)$_4$ (reprinted with permission from ref. 48, Copyright 2019 Royal Society of Chemistry).

multilayer photoanodes comprising Ag NCs and TiO_2 is worth proposing. For Ag NCs with suitable surface charge properties and energy band structure, potential derivatives may emerge in the future, and their roles in LbL-assembled PEC systems cannot be overlooked.

Compared with rod-shaped TNRAs, tubular porous TiO_2 nanotube arrays (TNTAs) have a larger specific surface area and more reactive sites, which can effectively improve the PEC performance.[49] For example, Xiao *et al.* used a facile and easily accessible LbL assembly strategy to uniformly deposit metal (Au, Ag, Pt) colloidal NPs on the TNTAs and investigated the effect of the number of deposition cycles on the PEC performances of TNTAs/metal NP heterostructures.[50] Specifically, PEC performances of the Au/TNTA heterostructure increase with the assembly cycle ($n = 1, 2, 4, 6\ldots$), reach an optimal value at $n = 8$, and decrease with increasing deposition layer to 10 layers. This result is because excessive deposition of metal NPs leads to unfavorable agglomeration, which hinders the active sites of TNTAs. Therefore, this work demonstrates that, for the LbL assembly system of metal NPs and TiO_2, an appropriate number of assembly cycles is the key factor affecting the PEC performances of the multilayer heterostructure photoanodes. As shown in Fig. 3e and f, in an analogous work, Hou *et al.* alternately deposited negatively charged transition metal chalcogenide (TMC) QDs and positively charged ultra-thin branched polyethyleneimine (BPEI) on the TNTA substrate, resulting in the TNTAs/(BPEI/CdX QDs)$_n$ (X = Se, Te, S) photoanodes.[48] The UV-visible diffuse reflectance spectroscopy (DRS) results indicate that, compared to the original TNTAs, the ternary heterostructures with different assembly cycles all exhibit enhanced light absorption, with the TNTAs/(BPEI/CdX QDs)$_8$ photoanode showing the strongest absorption. In addition, in a series of PEC tests, the TNTAs/(BPEI/CdX QDs)$_8$ multilayer photoelectrode exhibited significantly enhanced water oxidation activity under simulated solar irradiation. This enhanced solar energy conversion efficiency is attributed to the tight interfacial bonding mode between TMC QDs and TNTAs enabled by the LbL assembly technique, which maximizes the strong photosensitizing effects of TMC QDs. In addition to TNRAs and TNTAs, one-dimensional TiO_2 nanobelt (TNB) structures have also been utilized for LbL assembly construction. Specifically, Zhang *et al.* prepared the TNB substrate by a hydrothermal method, and then WO_3 nanowires (WO_3 NRs) were deposited on the TNBs by electrostatic attraction, and finally graphene oxide (GO) was attached on the TNBs/(WO_3 NRs) framework to obtain the TNBs/(WO_3 NRs/GO)$_n$ ternary nanohybrid heterostructures.[51] This study reveal that the TNBs/(WO_3 NRs/GO)$_n$ ternary composites exhibit the highest photocurrent density under visible light irradiation, which is attributed to the forming well-aligned Type-II energy level configuration between TNBs, WO_3, and GO afforded by LbL assembly. The LbL assembly technique enables close integration of WO_3 NRs and GR on the TNB scaffold, endowing the spatially multilayered nano-architecture with a cascade electron transfer channel that significantly accelerates charge transport. Consequently, rational selection of applicable functional building blocks in LbL assembly construction is of paramount importance.

4.1.2. WO_3. Tungsten trioxide (WO_3), exhibiting an intrinsic bandgap of 2.5–2.8 eV with visible light absorption extending to 500 nm, has been established as a robust photoanode candidate due to its exceptional physicochemical stability under both acidic conditions and photocorrosive environments.[52] For instance, Gonçalves *et al.* fabricated a WO_3 photoanode with a layer-stacked nanosheet architecture *via* a modified hydrothermal method and systematically investigated the correlation between the multilayer structure and its PEC performances.[53] The results indicated that the PEC water splitting performance of five-layer WO_3 was 70% higher than that of single-layer WO_3, and the authors determined that the fractal dimension of WO_3 nanosheets and their (220) crystal orientation are the key factors affecting the PEC water splitting efficiency of photoanodes. Wei *et al.* deposited multiple layers of CdSe QDs and poly(4-styrenesulfonic acid) (PSS) onto WO_3 nanoplate arrays (NPAs) using a LbL assembly approach.[54] As shown in Fig. 4a, positively charged CdSe QDs and negatively charged PSS were alternately deposited on the WO_3 NPA surface, with PSS acting as molecular glue to provide a tight face-to-face bonding mode between CdSe QDs and the WO_3 NPA substrate. The PEC water oxidation kinetics curve in Fig. 4b indicates that the transient time of the WO_3/(CdSe QDs/PSS)$_8$ multilayer photoanode is longer than that of the WO_3/(CdSe QDs)$_8$ photoanode. This suggests that insertion of the PSS intermediate layer induces electron tunneling between CdSe QDs and the WO_3 NPA substrate, ultimately suppressing the charge recombination and extending the charge lifetime of the photoanode. To further investigate the influence of the molecular structure of non-conjugated polymers on the electron tunneling effect, the PSS layer was replaced by a similar negatively charged non-conjugated polymer, *i.e.*, poly(vinyl sulfonic acid sodium salt) (PVAS). Notably, the PEC performances of the multilayer photoelectrode constructed with PVAS are comparable to those of the PSS-based photosystem, confirming the efficient role of electron tunneling in accelerating interfacial charge transfer and separation. In addition, the WO_3/(CdSe QDs/PSS)$_8$ multilayer photoanode maintains its optical absorption edge, elemental chemical state, and morphology without apparent change after 1 h of PEC reaction, suggesting the excellent stability of this spatially multilayered photoelectrode assembled *via* LbL assembly. To systematically analyze the long-term stability of this ideal assembly module, Wei *et al.* further introduced a small amount of hole scavenger into the electrolyte. The results show a significant improvement in photo-stability, revealing that holes are the critical factor affecting the photo-stability of the WO_3/(CdSe QDs/PSS)$_8$ multilayer photoanode.

In another work on sheet-like WO_3, Li *et al.* used an electrostatic LbL assembly strategy to deposit multilayers of PDDA and CdSe NCs on WO_3 substrates to obtain WO_3/(PDDA/CdSe)$_n$ heterostructured photoanodes.[55] The results manifest that the synergistic interaction between PDDA as an efficient electron transfer medium and CdSe NCs as a photosensitizer contributes to the cascade charge transfer channels, notably accelerating the interfacial charge transfer kinetics and boosting charge

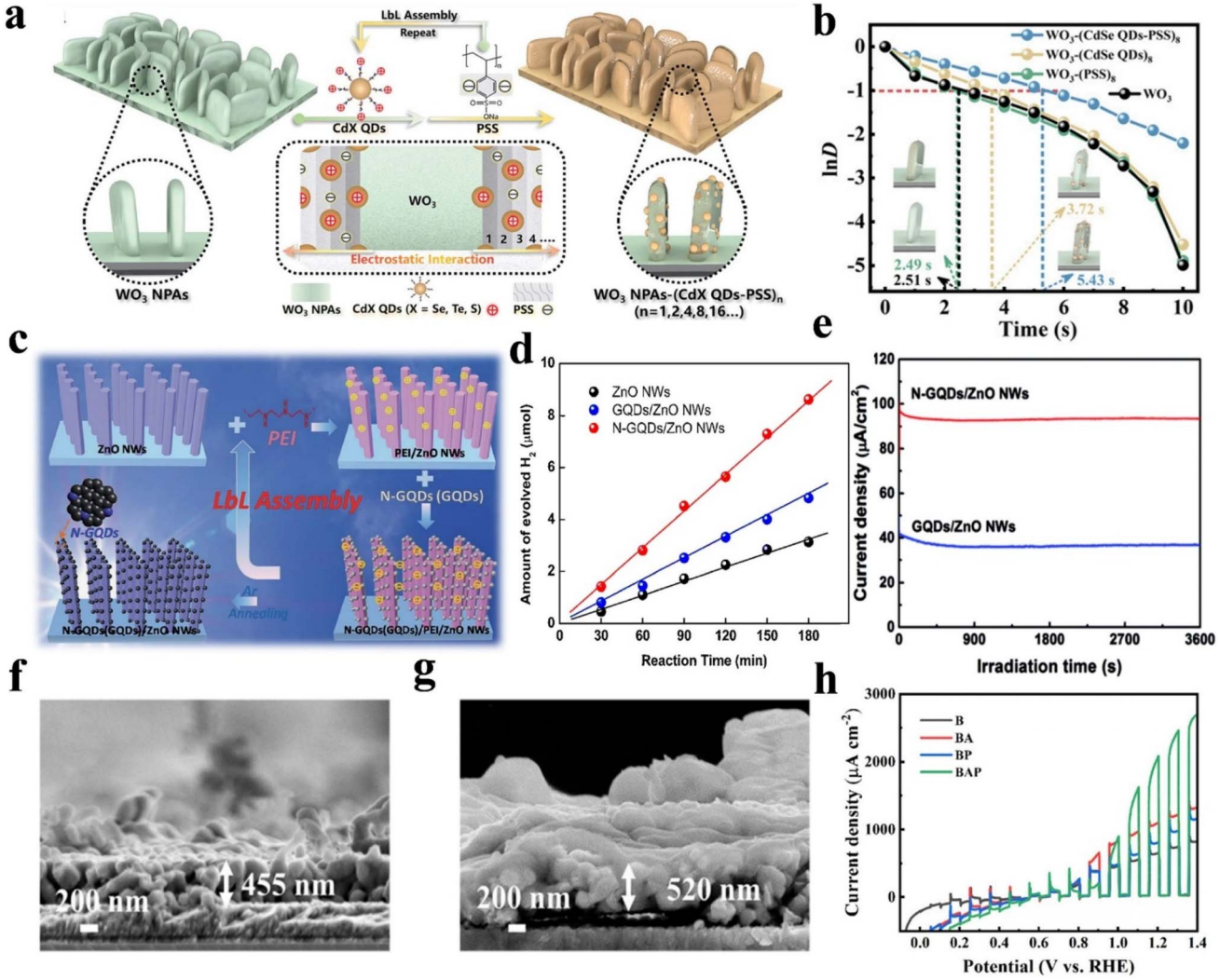

Fig. 4 (a) Schematic illustration of the LbL assembly process for WO_3 NPAs/(CdSe QDs/PSS)$_8$ photoelectrodes. (b) Transient kinetic curves of WO_3 NPAs/(CdSe QDs/PSS)$_8$ multilayer photoanodes (reprinted with permission from ref. 54, Copyright 2022 Wiley-VCH Verlag). (c) Schematic diagram illustrating the LbL assembly of N-GQD/ZnO NW photoelectrodes. (d) Hydrogen production performance of N-GQD/ZnO NWs under simulated sunlight (100 mW cm^{-2}). (e) Photostability of GQDs/ZnO NW and N-GQDs/ZnO NW heterostructures with zero bias *vs.* Ag/AgCl (reprinted with permission from ref. 57, Copyright 2016 Royal Society of Chemistry). Cross-sectional SEM images of (f) $BiVO_4$ and (g) $BiVO_4$/(Ag$_x$ NCs/PAH)$_8$ heterostructured photoanodes. (h) LSV curves of $BiVO_4$/(Ag$_x$ NCs/PAH)$_8$ photoelectrodes (reprinted with permission from ref. 58, Copyright 2024 American Chemical Society).

separation, definitively endowing the WO_3/(PDDA/CdSe)$_4$ multilayer photoanodes with exceptional PEC water oxidation performance under simulated and visible light irradiation. Furthermore, the formation of this cascade charge transfer channels originates from the LbL assembly strategy, which endows the tightly bound WO_3 and CdSe NCs with good energy level alignment. Specifically, PDDA and CdSe MSCs form highly ordered cascading electron transfer pathways, further accelerating the spontaneous transfer of photogenerated electrons from the LUMO of CdSe NCs to the CB energy level of WO_3 NPA, thereby enhancing charge transfer and separation efficiency. Besides the sheet-like WO_3 materials, Lin *et al.* assembled Au NPs on the WO_3 nanorods (NRs) *via* a facile LbL assembly approach to obtain the Au/WO_3 multilayer structure.[56] In this work, alternate deposition of PSS and PDDA imparts a positive charge to the WO_3 NR surface, enabling the LbL assembly with negatively charged Au NPs. The role of Au NPs as electron traps rather than plasmonic photosensitizers accelerates interfacial electron transfer, thereby extending the lifetime of photoinduced electron–hole pairs. Based on the above, considering the representative multilayer photoanodes fabricated *via* LbL assembly incorporating WO_3 and CdSe, where WO_3 serves as an ideal substrate model with excellent stability, future research would greatly enhance this ideal model by introducing more controllable building blocks.

4.1.3. ZnO. Zinc oxide (ZnO) is a direct bandgap semiconductor with a bandgap of approximately 3.37 eV and an exciton binding energy as high as 60 meV.[59] Its excellent electron mobility and thermal conductivity make it an ideal material for photoelectrode preparation. However, ZnO exhibits

several inherent limitations, including rapid carrier recombination, a wide bandgap that confines its light absorption to the ultraviolet region, and insufficient chemical stability in an electrolyte solution.[60] To address these issues, Sun *et al.* integrated Au@ZnO core–shell NPs into a 2D array film using a LbL assembly approach.[61] The Au NPs exhibit a surface plasmon resonance (SPR) effect, which extends the light absorption range of ZnO to the visible spectrum. Yuan *et al.* combined positively charged ZnO NPs with negatively charged TiO_2 NPs using a LbL assembly method to prepare ZnO/TiO_2 multilayered films.[62] This does not require any polyelectrolytes and results in a film composed entirely of nanoparticles with a tightly coupled heterojunction, enhancing the PEC water splitting performances by a factor of five compared with pure TiO_2. As shown in Fig. 4c, Zeng and his colleagues used a facile LbL assembly strategy to load nitrogen-doped graphene QDs (N-GQDs) onto ZnO nanowires (NWs), resulting in the N-GQDs/ZnO NWs heterostructure.[57] Under simulated sunlight irradiation, the N-GQDs/ZnO NW photoanode exhibits superior PEC performances and stability compared with pure ZnO NWs and nitrogen-free GQDs/ZnO NWs counterparts (Fig. 4d and e). This significant enhancement is attributed to the contribution of amine groups in BPEI, which endows it with high affinity to the hydrophilic ZnO NW surface, resulting in a tightly coupled interface between N-GQDs and ZnO, facilitating the favorable energy level alignment. Additionally, compared with N-GQDs/ZnO nanocomposites prepared by traditional coating methods, the LbL-assembled N-GQDs/ZnO NWs heterostructure photoanode shows a threefold increase in photocurrent density. This result confirms that the LbL assembly strategy enables the fine control of the face-to-face integration mode between building blocks at the microscopic interface, optimizing the material advantages of functional components.

4.1.4. $BiVO_4$. Bismuth vanadate ($BiVO_4$) possesses a bandgap of 2.4 eV, with its VB edge positioned at approximately 2.7 V *vs.* RHE.[63] This potential is sufficiently positive to thermodynamically drive the oxygen evolution reaction (OER, 1.23 V *vs.* RHE).[64] Moreover, $BiVO_4$ exhibits robust chemical stability under neutral and alkaline conditions, rendering it an ideal photoanode material for PEC water splitting.[65] However, low charge transfer efficiency and rapid charge recombination limit its STH conversion efficiency.[66] To enhance the PEC performances of $BiVO_4$, Chang *et al.* deposited a multilayered ultrathin Al_2O_3 coating on the $BiVO_4$ surface.[67] This work demonstrated that Al_2O_3 effectively passivates the surface trap states in $BiVO_4$, thereby suppressing electron–hole recombination over $BiVO_4$. In another case, Chen *et al.* utilized a LbL assembly method to alternately deposit Ag_x NCs and poly(-allylamine hydrochloride) (PAH) onto the $BiVO_4$ substrate, forming $BiVO_4$/(Ag_x NCs/PAH)$_n$ heterostructures (Fig. 4f and g).[58] Compared with the bare $BiVO_4$ and $BiVO_4$/(Ag_x NCs)$_n$ counterparts, $BiVO_4$/(Ag_x NCs/PAH)$_n$ photoanodes exhibited markedly enhanced PEC water oxidation performances under visible light irradiation (Fig. 4h). It is noteworthy that solid PAH, due to the absence of delocalized π electrons in its molecular structure, cannot participate in the charge transfer process and is typically regarded as an insulating polymer. Consequently, charge transfer resistance of the $BiVO_4$/(PAH)$_n$ photoanode shows almost no change compared with $BiVO_4$. However, in this work, the $BiVO_4$/(Ag_x NCs/PAH)$_n$ photoanode exhibits a significant enhancement in PEC performances compared with the $BiVO_4$/(Ag_x NCs)$_n$ photoanode without PAH. This improvement is attributed to the electron tunneling effect provided by PAH, which facilitates the smooth transfer of photoexcited electrons from Ag_x NCs to the $BiVO_4$ substrate, stimulating an unexpected cascade charge transfer pathway. Additionally, the well-matched energy level structure between Ag_x NCs and $BiVO_4$ is a crucial factor for yielding this charge transfer route.

4.1.5. CdS. Cadmium sulfide (CdS) possesses a bandgap of 2.4 eV, and its CB edge (−1.0 V *vs.* RHE) is more negative than the H^+/H_2 reduction potential (0 V *vs.* RHE),[68] while its VB edge (1.4 V *vs.* RHE) is more positive than the water oxidation potential (1.23 V *vs.* RHE).[69] These properties enable CdS to drive both the HER and OER simultaneously, rendering it an ideal candidate for PEC water splitting.[70] For example, Li *et al.* fabricated multilayered CdS/(BPEI/MoS_2)$_n$ heterostructures by sequentially depositing positively charged branched polyethyleneimine (BPEI) and negatively charged MoS_2 QDs onto CdS NWs using a LbL assembly approach.[71] In this multilayer structure, BPEI possesses various amino groups grafted onto its branched molecular chain, enabling coordination with transition-metal ions. Consequently, in the final bilayer, they replaced pure BPEI with transition-metal ion-coordinated BPEI (TMI-BPEI), yielding the CdS/(TMI-B/M)$_4$ multilayer heterostructure. Compared with pristine CdS NWs, both the CdS/(TMI-B/M)$_4$ and CdS/(BPEI/MoS_2)$_4$ multilayer heterostructures exhibited significantly enhanced HER performances under visible light irradiation. During the photogenerated charge transfer process, as the thickness of BPEI is much smaller than the mean free path of electron transport, electron transfer from CdS NWs to MoS_2 QDs by tunneling through the ultrathin BPEI layer was unaffected. Moreover, due to Cu^{2+} ions being coordinated and anchored onto the molecular side chains of BPEI, which are alternately and closely stacked with MoS_2 QDs, direct contact between the Cu^{2+} ions and MoS_2 QDs is ensured. Benefiting from the unique face-to-face stacking mode of CdS NWs and MoS_2 QDs imparted by the LbL assembly strategy, BPEI acts as an effective hole-capturing medium, thereby constructing efficient cascade hole transfer channels. In addition, the transition-metal ions (Fe^{2+}, Co^{2+}, Ni^{2+}, Cu^{2+}, Zn^{2+}) serve as interfacial electron transfer mediators, accelerating electron transfer toward active sites. The remarkably improved interfacial electron transfer kinetics in this study strongly demonstrates the innovation and efficiency of the LbL assembly technique in precisely controlling the interfacial structure between building blocks.

4.2. LbL assembly with quantum dots as building blocks

As 0D nanomaterials, QDs exhibit unique PEC properties closely related to their size.[72] The size of QDs is comparable to or smaller than the exciton Bohr radius of their bulk materials, showing a pronounced quantum size effect and allowing precise bandgap tuning by controlling the particle size.

Therefore, in LbL assembly, QDs enable forming suitable energy level alignment with the substrate materials, thereby enhancing the charge transport between different building blocks and thus improving the PEC water splitting performances. Additionally, QDs possess a high surface-to-volume ratio and exhibit a quantum tunneling effect, making them ideal building blocks for constructing multilayered photoanodes.[22a] This section provides a comprehensive overview of high-efficiency photoelectrodes fabricated using diverse QDs including TMC QDs, graphene QDs, and MXene QDs as primary building blocks for LbL assembly.

4.2.1. TMC QDs. TMC consist of transition metals (*e.g.*, Cd, Ti, Mo, W) coordinated with chalcogen elements (S, Se, Te).[73] Structurally, TMC feature a sandwich-like arrangement where a transition metal layer is interposed between two chalcogen atom layers.[74] Within each layer, atoms are bonded *via* strong covalent interaction, whereas adjacent layers are bound by weak van der Waals force.[75] TMC QDs typically exhibit a narrow bandgap below 2.4 eV, for example, CdSe, CdTe, and MoS_2 QDs display bandgaps of 1.7 eV, 1.4 eV, and 1.9 eV, respectively.[76] Such a narrow bandgap improves the solar energy absorption, making TMC excellent light-harvesting antennas.[77] For instance, Hou *et al.* utilized LbL assembly to deposit CdTe QDs with tailored surface charges onto a TNTA substrate.[78] CdTe QDs functionalized with 2-aminoethanethiol (AET) exhibit a positive surface charge, while those modified with mercaptoacetic acid (MAA) demonstrate a negative charge (Fig. 5a). The DRS results of two differently ligand-capped CdTe QDs show significant light absorption at $\lambda < 550$ nm. Furthermore, IPCE measurements demonstrate that the light absorption edge of TNTAs/(CdX@AET QDs/CdX@MAA QDs)$_n$ photoanodes extends to 550 nm compared with pristine TNTAs. These results confirm

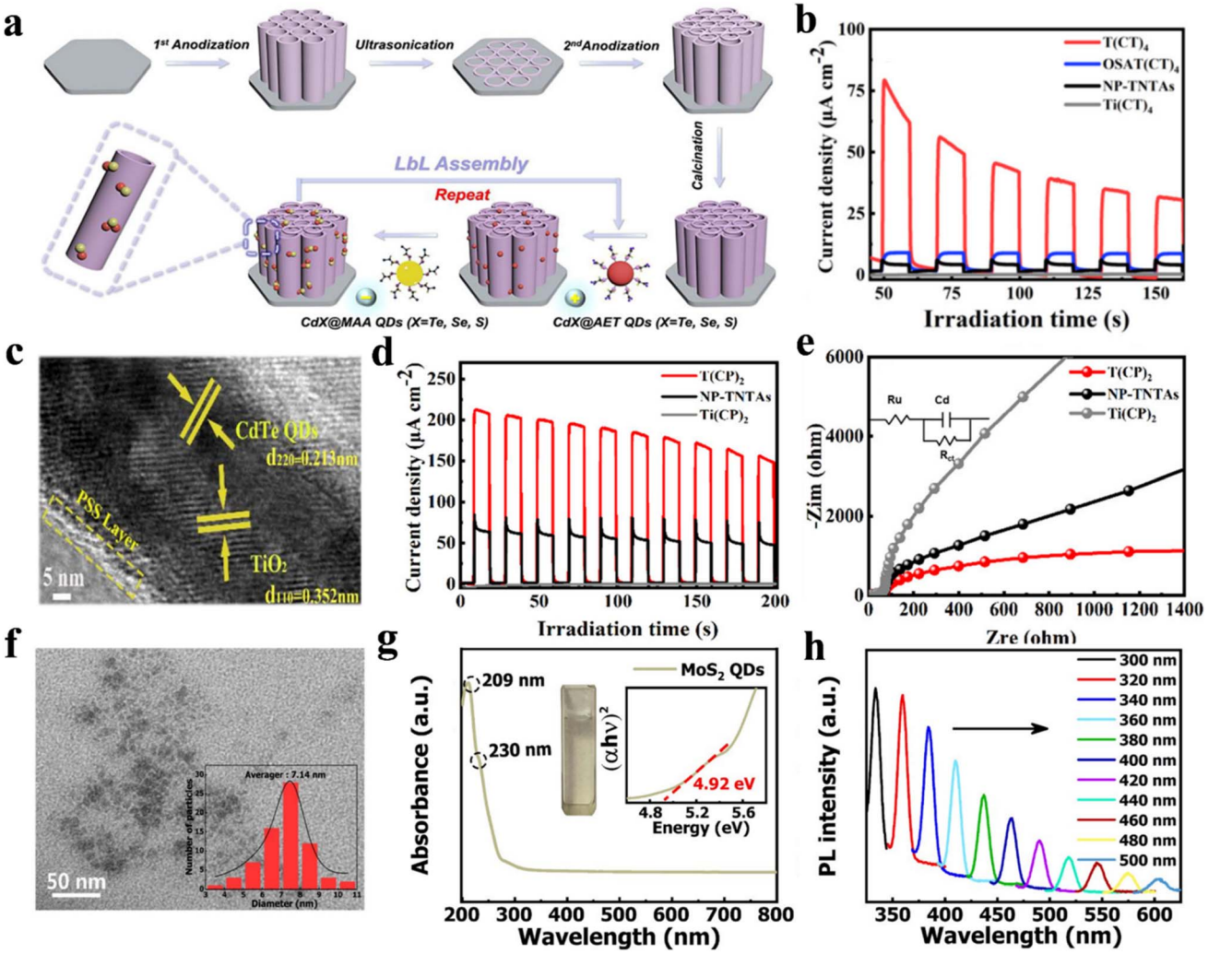

Fig. 5 (a) Schematic illustration for LbL assembly of TNTAs/(CdX@AET QDs/CdX@MAA QDs)$_n$ multilayered photoanodes. (b) *I*–*t* curves of TNTAs/(CdX@AET QDs/CdX@MAA QDs)$_n$ photoanodes (reprinted with permission from ref. 78, Copyright 2021 American Chemical Society). (c) HR-TEM images of TNTAs/(TMC QDs/PSS)$_2$ photoanodes. (d) *I*–*t* curves and (e) EIS results of TNTAs/(TMC QDs/PSS)$_2$ photoanodes under visible light irradiation (reprinted with permission from ref. 79, Copyright 2020 American Chemical Society). (f) TEM image of MoS_2 QD aqueous solution and histogram of size distribution. (g) UV-Vis absorption spectra of MoS_2 QD aqueous solutions, as well as photographs and bandgap energy measurements. (h) PL spectra of MoS_2 QD aqueous solution at different excitation wavelengths (reprinted with permission from ref. 80, Copyright 2020 Royal Society of Chemistry).

the successful deposition of CdX QDs and demonstrate the effectiveness of the LbL assembly technique for integrating diverse materials. To further optimize charge transport, Hou *et al.* further developed composite photoanode systems combining TMC QDs with non-conjugated polymers. As shown in Fig. 5c and d, TMC QDs [CdX (X = Se, Te, S)] and poly(4-styrenesulfonic acid) (PSS) were alternately deposited onto a TNTA substrate, forming the TNTAs/(TMC QDs/PSS)$_n$ photoanodes.[79] The ultrathin PSS interlayers acted as "molecular glue", enabling the precise and ordered assembly of TMC QDs on the TNTA substrate. The results indicate that the TNTAs/(TMC QDs/PSS)$_n$ multilayer photoanode exhibits the highest photocurrent density and the lowest interfacial charge transfer resistance (Fig. 5d and e). This is mainly due to the effective deposition of TMC QDs by LbL assembly technology, which produces a unidirectional cascade charge transfer path, resulting in the smooth transmission of electrons from TMC QDs to TNTAs, and promoting charge separation/migration. In another example of combining TMC QDs with non-conjugated polymers for fabricating photoanodes, Wei *et al.* used the LbL assembly technique to integrate MoS_2 QDs with BPEI on the TNTAs, forming multilayer TNTAs/(BPEI/MoS_2)$_n$ ternary heterostructures (Fig. 5f–h).[80] Relevant information for the MoS_2 QDs is shown in Fig. 5f–h. Although MoS_2 QDs do not exhibit strong light absorption properties compared with CdX QDs, their role in promoting electron transfer in fields such as photocatalysis and PEC water splitting is significant. The linear sweep voltammetry (LSV) and Mott–Schottky measurements revealed that the TNTAs/(BPEI–MoS_2)$_n$ photoanode exhibited a superior charge transfer rate compared to both the single-component and binary counterparts. Notably, within such a multilayer structure, the inherently positively charged surface and strong reducibility of BPEI enable the ultrathin BPEI layer to function as an efficient hole-capturing medium, while the MoS_2 QD layer acts as an electron-extracting medium. Therefore, BPEI and QDs collectively form two spatially isolated charge transfer channels within the multilayer photoanode, thereby significantly enhancing the PEC performances.

4.2.2. Graphene QDs. Graphene, a quintessential 2D material, features a hexagonal carbon lattice with a honeycomb structure.[81] Graphene quantum dots (GQDs), derived from 2D graphene, retain their remarkable properties, including ultrahigh electrical conductivity (~2000 S m^{-1}) and extraordinarily high specific surface area (~2630 m^2 g^{-1}).[82] Furthermore, the abundant oxygen-containing functional groups (–COOH, –OH) on the GQD surface, combined with excellent electrochemical stability, make GQDs ideal building blocks for preparing photoelectrodes using LbL assembly technology.[83] For instance, Zeng *et al.* employed a LbL assembly strategy to fabricate (M/GQDs)$_n$ (M = Au, Ag, Pt) multilayer photoanodes (Fig. 6a and b), where GQDs and metal NPs alternately deposited on a fluorine-doped tin oxide (FTO) glass substrate *via* electrostatic interaction.[84] The DRS results of both (Au/GQDs)$_n$ and (Ag/GQDs)$_{10}$ multilayer thin films concurrently exhibit two peaks at 355 nm and 530/410 nm, attributed to the typical absorption peaks of GQDs and the SPR peaks of Au/Ag NPs, respectively. Furthermore, the absorption intensities of these two peaks increase proportionally with the number of assembly cycles, demonstrating the progressive growth of the (Au/GQDs)$_n$ multilayer films and confirming that the LbL assembly technique can construct multilayer spatial structures with precisely alternating integration. Notably, compared with single-component metal NPs or GQDs, the (Au/GQDs)$_{10}$ photoelectrode exhibits significantly enhanced photocurrent density and retains 80% of its initial photocurrent after 30 min of continuous simulated sunlight irradiation. This indicates that, despite lacking critical adsorption support from a substrate material, the heterogeneous interface between Au NPs and GQDs integrated through electrostatic LbL assembly technology can still be effectively stabilized. Building upon this study, researchers further integrated GQDs and Ag NPs on the TNRAs *via* LbL assembly, resulting in the formation of TNRAs/(Ag NPs/GQDs)$_n$ multilayer photoelectrodes.[85] Notably, owing to the photosensitizing capability of GQDs and surface plasmon resonance effect of Ag NPs, the light absorption range of TNRAs is extended to *ca.* 800 nm. PEC results reveal that compared with unitary or binary counterparts, TNRAs/(Ag NPs/GQDs)$_n$ exhibits markedly enhanced photocurrent and significantly reduced interfacial charge transfer resistance. Such improvements are attributed to the favorable band alignment formed between GQDs and TiO_2, as well as the *in situ* formation of plasmonic Ag NPs facilitating hot electron generation. As a result, Ag NPs act as an efficient charge transfer medium, triggering cascade and smooth electron transfer from GQDs to TiO_2, thereby significantly prolonging the carrier lifetime. Consequently, it is worth mentioning that in both studies on GQDs and metal NPs, LbL assembly enables unique and stable face-to-face intimate integration of GQDs and metal NPs. This meticulously engineered interfacial architecture is pivotal to maximizing the synergistic photogenerated charge interactions between the two components.

4.2.3. MXene QDs. The chemical formula of MXene precursors is generally denoted as $M_{n+1}AX_n$ (n = 1–4), where M represents the transition metals from Groups IIIB–VIB (*e.g.*, Ti, Sc, V, Mo), A is typically the element from Groups IIA or IVA (*e.g.*, Al, Si, In), and X represents either C or N.[87] 2D layered MXene materials exhibit metallic-level conductivity, stable chemical properties, and abundant surface active sites, making them widely applicable for photoelectrocatalysis.[88] For example, Yan's group deposited multilayer $Ti_3C_2T_x$ films onto $BiVO_4$ photoanodes, resulting in a significant enhancement in photocurrent density and photoconversion efficiency. This suggests that integration of MXenes with semiconductors in fabricating photoelectrodes effectively promotes the separation of electron–hole pairs.[89] Moreover, rational assembly of MXene QDs (MQDs) with semiconductors enables precise control over the structure of the resulting photoelectrodes at the nanoscale. For instance, Li *et al.* utilized a LbL assembly technique to alternately deposit Ti_3C_2 QDs and non-conjugated polymer PDDA on the TNRA substrate.[24] The resulting TiO_2/(PDDA/MQDs)$_6$ photoelectrodes show 92% charge injection and 60% separation efficiencies (1.23 V *versus* RHE), which significantly outperforms bare TNRAs with 88% and 56% (Fig. 6d), respectively. This enhancement is attributed to the good energy level alignment

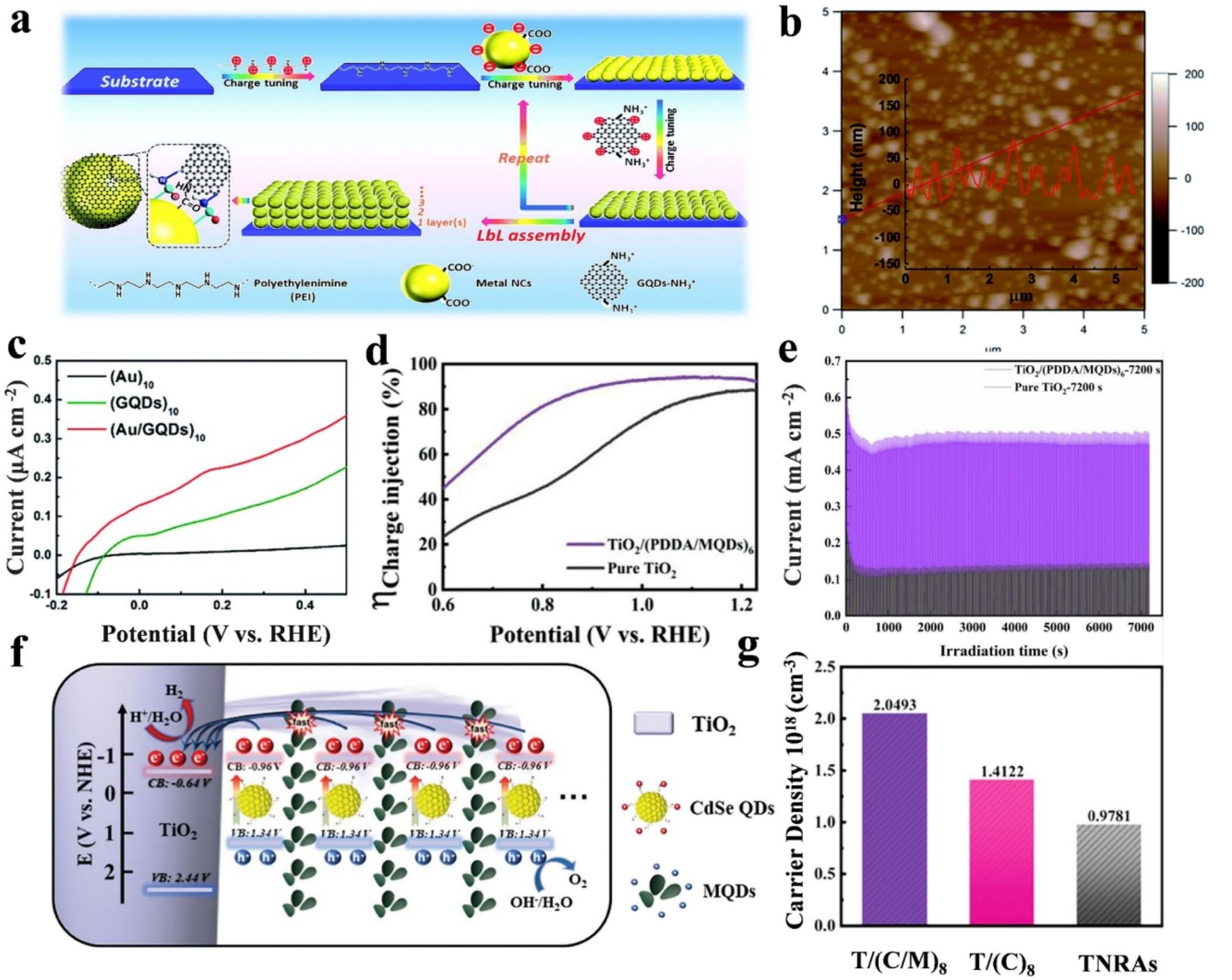

Fig. 6 (a) Schematic illustration of the LbL assembly process for the fabrication of $(M/GQDs)_n$ (M = Au, Ag, Pt) multilayer thin films. (b) Atomic force microscopy (AFM) image and (c) LSV curves of the $(Au/GQDs)_{10}$ multilayer film (reprinted with permission from ref. 84, Copyright 2017 Royal Society of Chemistry). (d) Charge injection efficiency of $TiO_2/(PDDA/MQDs)_6$ and TiO_2 photoanodes. (e) Photocurrents of $TiO_2/(PDDA/MQDs)_6$ and TiO_2 photoanodes under continuous simulated sunlight irradiation (AM 1.5G) (reprinted with permission from ref. 24, Copyright 2023 Wiley-VCH Verlag). (f) Schematic illustration depicting the PEC water oxidation mechanism of TNRAs/(TMC QDs/$MQDs)_8$ photoanodes. (g) Carrier densities of TNRAs, TNRAs/(TMC $QDs)_8$ and TNRAs/(TMC QDs/$MQDs)_8$ photoanodes (reprinted with permission from ref. 86, Copyright 2024 Wiley-VCH Verlag).

between TiO_2 and MQDs, which enables the spontaneous transfer of photoexcited electrons in TiO_2 to MQDs. More importantly, PDDA and MQDs, as coexisting electron capture media, synergistically form a cascade electron transfer chain that accelerates the directional transfer of photogenerated electrons. Notably, in terms of stability, $TiO_2/(MQDs)_6$ and $TiO_2/(PDDA)_6$ exhibited inferior stability under continuous simulated sunlight irradiation compared with pure TNRAs. However, $TiO_2/(PDDA/MQDs)_6$ demonstrated relatively good stability even after 2 h of solar light irradiation (Fig. 6e). This strongly indicates the substantial electrostatic binding force between oppositely charged PDDA and MQDs during the LbL assembly process, which prevents the spatially multilayered heterostructure from dissolving or degrading in the PEC water oxidation reaction. This study revealed the crucial role of MXenes as co-catalysts in enhancing interfacial charge transfer during the PEC water splitting reaction. Besides this, Su *et al.* assembled TMC QDs and MQDs on the TNRAs using LbL assembly to construct the multilayer TNRAs/(TMC QDs/$MQDs)_n$ photoelectrodes.[86] In this artificial photosystem, the photosensitization effect of TMC QDs significantly extended the light absorption range of TNRAs to the visible spectrum region (Fig. 6f). Furthermore, by altering the assembly sequence of CdSe QDs and MQDs during the fabrication process, the distinctive spatial structural advantages conferred by the LbL assembly technique were further validated. The photocurrents of different structured photoanodes demonstrate that the assembly mode following a rational and unified principle more effectively utilizes the synergistic effect between CdSe QDs and MQDs to construct cascaded charge transfer pathways, thereby

accelerating charge transfer and separation. These works provided strong evidence that construction of the directional charge transfer route *via* LbL assembly is beneficial for enhancing the PEC water oxidation efficiency of spatially multilayered photoanodes.

4.3. LbL assembly with nanoclusters as building blocks

4.3.1. Metal nanoclusters. Metal nanoclusters (MNCs) have garnered significant attention in the field of photoelectrocatalysis due to their unique quantum confinement effect and abundant active sites.[90] When the size of MNCs (0.2–2 nm) approaches the Fermi wavelength of electrons (approximately 2 nm for gold), MNCs exhibit discrete energy levels similar to semiconductors.[91] For example, the highest occupied molecular orbital (HOMO) and lowest unoccupied molecular orbital (LUMO) levels of Au_{25}@$(GSH)_{18}$ are determined to be +1.90 and −0.42 V *vs.* NHE, respectively.[23,92] Atomic-level size control in MNCs achieves dual functionality including precise bandgap tuning and exposed surface with catalytically active sites, which collectively enhance the PEC water splitting efficiency.[93] Notably, functionalized ligand-modified MNCs exhibit robust stability and controllable surface charge, making them ideal building blocks for LbL assembly.[94] For instance, Mo *et al.* used LbL assembly to deposit negatively charged Au_x@GSH NCs and positively charged BPEI on the TNTA substrate, as shown in Fig. 7e and f.[95] The results showed that Au_x@GSH NCs as photosensitizers effectively extended the light absorption range of TNTAs. To further enhance the photostability of the composite photoanodes, they introduced different scavengers including *tert*-butanol, benzoquinone, and triethanolamine to selectively quench ·OH, $\cdot O_2^-$, and holes, respectively. Their

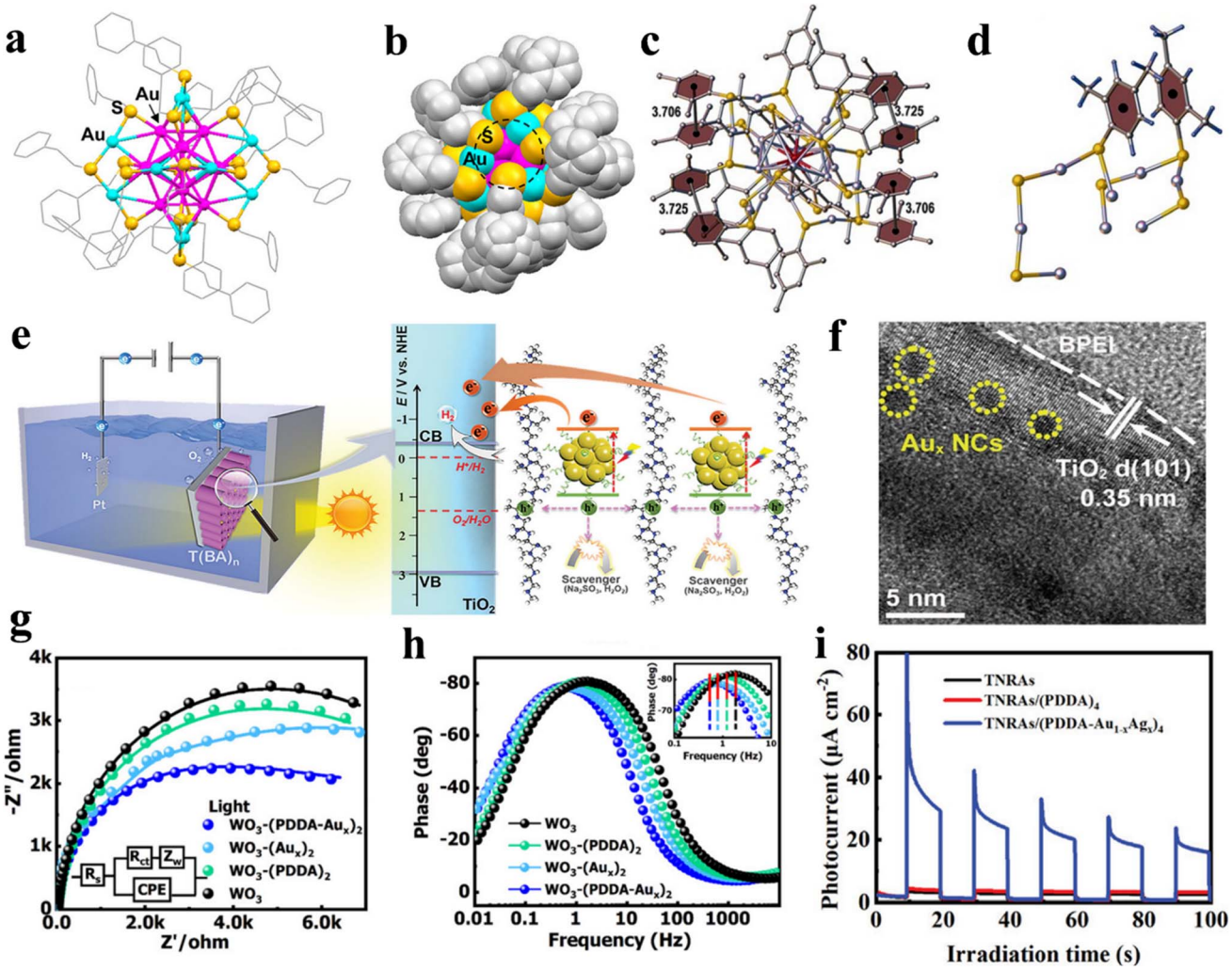

Fig. 7 (a) Ball-and-stick and (b) space-filling models of $Au_{25}(SCH_2CH_2Ph)_{18}$ NCs (reprinted with permission from ref. 98, Copyright 2013 American Chemical Society). (c) X-ray crystal structure and (d) methyl group orientations of $[Ag_{24}Au(SPhMe_2)_{18}]^-$ (reprinted with permission from ref. 99, Copyright 2015 Wiley-VCH Verlag). (e) Schematic diagram of the PEC water splitting mechanism for TNTAs/(BPEI–Au_xNCs)$_2$ photoanodes. (f) HRTEM image of the TNTAs/(BPEI/Au_xNCs)$_2$ heterostructure photoanode (reprinted with permission from ref. 95, Copyright 2023 Wiley-VCH Verlag). (g) EIS results and (h) Bode plots of WO_3/(PDDA/Au_x)$_2$ (reprinted with permission from ref. 23, Copyright 2020 American Chemical Society). (i) *I*–*t* curves (bias: 1.0 V *vs.* RHE) of TNRAs/(PDDA/$Au_{1-x}Ag_x$ NCs)$_4$ multilayer photoanodes (reprinted with permission from ref. 97, Copyright 2023 Wiley-VCH Verlag).

findings revealed that holes were the primary culprits responsible for the poor photostability of Au_x@GSH NCs. It is noteworthy that the DRS and TEM results of the TNTAs/Au_x NCs nanocomposite after continuous light irradiation clearly demonstrate the *in situ* self-transformation of Au_x@GSH NCs into Au nanoparticles, whereas Au_x@GSH NCs in the TNTAs/$(BPEI/Au_x\ NCs)_2$ multilayer heterostructure remain intact. The result strongly highlights the pivotal role of the non-conjugated polymer BPEI in protecting metal NCs and further confirms that the unique face-to-face integration mode and robust electrostatic interaction in LbL assembly are key to constructing high-performance heterostructures. The same group further investigated the synergistic effect of Au_x@GSH NCs and PAH on the solar water oxidation performance, both of which are utilized as the primary building blocks for LbL assembly.[96] Notably, compared with the TNTAs/$(BPEI/Au_x\ NCs)_2$ multilayer photoanode, in the TNTAs/$(Au_x\ NCs/PAH)_8$ multilayer structure, PAH serves as an insulating layer that does not participate in the interfacial charge transfer process between the TiO_2 substrate and Au_x NCs. Instead, it functions as an effective electron tunneling module, establishing a sequential charge transfer pathway. Furthermore, this electron tunneling-mediated charge transfer mechanism has been demonstrated to be universally applicable to various nanoclusters, including Au_x NCs, Ag_x NCs, and Au_{25} NCs. Similarly, Wei *et al.* deposited Au NCs (Au_x@GSH NCs and Au_{25}@GSH NCs) and PDDA on metal oxides (MOs: WO_3, Fe_2O_3, TiO_2) for constructing multilayer composite photoanodes.[23] Interestingly, the charge transfer resistance of the $WO_3/(PDDA)_2$ photoanode under illumination and in the dark exhibited opposite trends compared with bare WO_3, confirming the crucial role of PDDA as an electron transfer mediator in suppressing charge recombination (Fig. 7g and h). Furthermore, by further loading Au NCs *via* LbL assembly, the obtained ternary structure achieved a 1.8-fold increase in photocurrent density compared with $WO_3/(PDDA)_2$, demonstrating the effectiveness of the cascade charge transfer chain in the multilayer spatial structure.

In addition to Au NCs, Tang *et al.* also comprehensively explored the efficient role of multilayer Ag NCs [Ag_x@GSH, Ag_9@GSH, Ag_{16}@GSH, and Ag_{31}@GSH NCs] and PDDA deposition on the TNRA substrate.[47] Compared with bare TNRAs, the LbL-assembled TNRAs/$(PDDA/Ag\ NCs)_4$ heterostructure exhibits significantly enhanced carrier density, which is attributed to the role of PDDA as an efficient electron-trapping mediator that accelerates the charge transfer between the adjacent Ag NCs. Compared with monometallic NCs, alloy NCs composed of multiple metal atoms exhibit more intriguing PEC properties. For instance, Su *et al.* utilized a LbL assembly technique to alternately deposit $Au_{1-x}Ag_x$@GSH NCs and PDDA on the TNRA substrate.[97] As shown in Fig. 7i, the TNRAs/$(PDDA/Au_{1-x}Ag_x\ NCs)_4$ photoanodes exhibited significantly elevated photocurrent compared with the unexcited TNRA photoanodes under visible light irradiation. Furthermore, the PEC water splitting performances of TNRAs/$(PDDA/Au_{1-x}Ag_x\ NCs)_n$ photoanodes with varied LbL assembly sequences were also systematically investigated. The results suggested that the LbL assembly sequence could profoundly influence the electron transfer pathway and thereby enable precise control over charge separation and transfer between MNCs and metal oxides. However, it should be considered that TNRAs/$(PDDA/Au_{1-x}Ag_x)_4$ demonstrated limited photostability due to the deactivation of $Au_{1-x}Ag_x$@GSH NCs caused by superoxide radical oxidation. Therefore, for various alloy NCs (AuPt, AuCu), how to design multilayer structures that can protect the active metal atoms remains an important area for further investigation, similar to the specific protective effect of BPEI on Au_x NCs. This series of studies on MNCs highlights the universal significance of constructing a directional charge transfer route *via* LbL assembly, providing valuable insights for the rational design of MNC-based photoelectrodes. It is worth emphasizing that these MNCs with well-defined energy level structures and atomic configurations demonstrate universal compatibility with MOs. The assembly model of "MOs/non-conjugated polymer/MNCs", which establishes a well-oriented charge transfer pathway, can provide systematic theoretical guidance for the future design and optimization of LbL-assembled PEC devices.

4.3.2. Polyoxometalate nanoclusters. Polyoxometalates (POMs) are multinuclear metal-oxo clusters formed by high oxidation state transition metals (*e.g.*, Mo^{6+}, W^{6+}, V^{5+}) bridged through oxygen atoms.[100] These compounds exhibit a variety of well-defined topological structures, among which the most common one is the Keggin structure (*e.g.*, $[PMo_{12}O_{40}]^{3-}$) that features a central phosphorus atom surrounded by a cage-like framework of $12MoO_6$ octahedra interconnected *via* oxygen bridges (Fig. 8a).[101] The metal–oxygen units with high charge density on POM surfaces drive the adsorption of reactant molecules or ions *via* electrostatic interaction or hydrogen bonding, thereby facilitating multi-electron redox reactions.[102] As nanoscale anionic clusters with reversible multi-electron redox activity and proton-coupled electron transfer capabilities, POMs can serve as ideal building blocks in LbL assembly for fabricating photoelectrodes with enhanced charge separation efficiency.[103] As shown in Fig. 8b, Wu *et al.* employed a LbL assembly strategy to load hexavalent manganese polyoxometalates (Mn_6SiW) and graphite phase carbon nitride (g-C_3N_4) nanosheets on the indium tin oxide (ITO) electrode, thereby fabricating low-cost Mn_6SiW/g-C_3N_4 composite photoelectrodes.[104] The results suggest that the photocurrent density of the composite photoelectrode was twice that of the pure g-C_3N_4 photoelectrode. Furthermore, the photocurrent density increased with an increasing number of composite film layers. This enhancement was attributed to the Mn–O clusters in Mn_6SiW, which efficiently reduce the oxygen evolution overpotential and promote the PEC water splitting reaction. Notably, Mn_6SiW exhibits relatively low cost, while the LbL assembly technique enables tight interfacial integration between Mn_6SiW and pristine g-C_3N_4, thereby maximizing the material advantages of Mn_6SiW. Pei *et al.* constructed the PDDA/$[Ni_{25}$-POM/(PDDA-rGO)$]_n$ photoanodes through alternating deposition of Ni-substituted POM (Ni_{25}-POM) and PDDA-functionalized reduced graphene oxide (PDDA-rGO) on ITO.[105] The results demonstrated that the PDDA/$[Ni_{25}$-POM/(PDDA-rGO)$]_n$ photoelectrodes exhibited excellent activity and stability, with water oxidation current 1.7 times higher than that of the

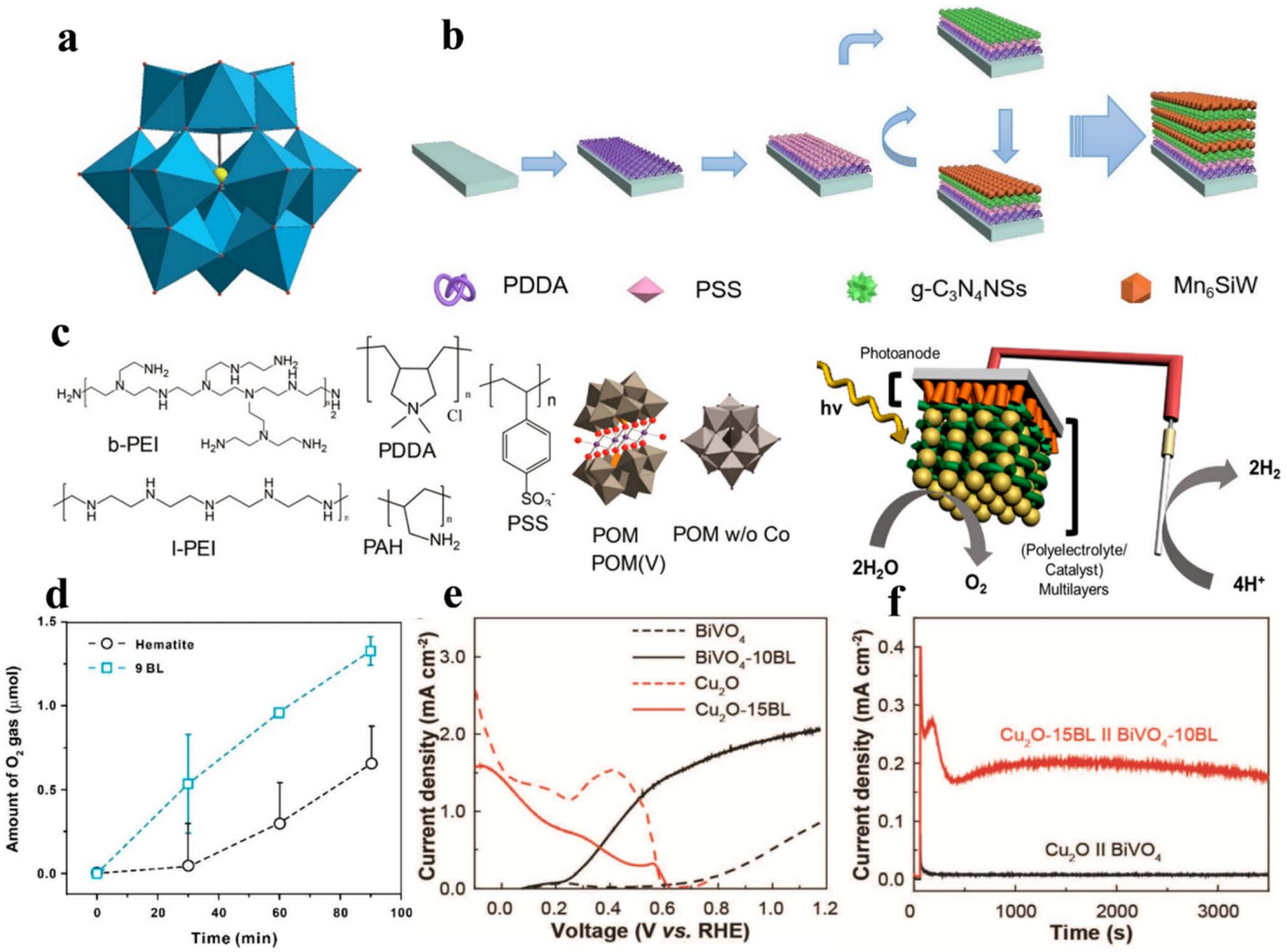

Fig. 8 (a) Model diagrams of classic Keggin anion $[XM_{12}O_{40}]^{3-}$ (X = P, Si, Bi, *etc.*, M = Mo, W, V, Nb, *etc.*) (reprinted with permission from ref. 101, Copyright 2018 Springer Nature). (b) Diagram depicting the LbL assembly of Mn_6SiW and g-C_3N_4 composite films (reprinted with permission from ref. 104, Copyright 2021 Multidisciplinary Digital Publishing Institute). (c) Schematic diagram of photoanodes prepared using different polyelectrolytes and metal oxides (reprinted with permission from ref. 107, Copyright 2017 American Chemical Society). (d) OER performance of an Fe_2O_3/(Co-POM/GO)$_n$ multilayer photoanode (reprinted with permission from ref. 108, Copyright 2018 American Chemical Society). (e) LSV curves and (f) stability of Cu_2O and $BiVO_4$ PEC cells (reprinted with permission from ref. 109, Copyright 2018 Royal Society of Chemistry).

control [PDDA/Ni_{25}-POMs]$_n$ photoanodes at equivalent layers. This improvement is attributed to favorable electronic interactions resulting from the advantageous energy level alignment between Ni_{25}-POMs and rGO, where rGO accelerates electron transport and suppresses charge recombination. Similarly, Zhou *et al.* employed a LbL assembly approach to deposit Mn_4-containing silicotungstate (Mn_4-POM), PDDA, and Co_3O_4, resulting in the construction of PDDA/(Mn_4-POM/Co_3O_4)$_4$/Mn_4-POM multilayer photoanodes.[106] In this composite structure, Mn_4-POM effectively promotes the transfer of photogenerated electrons from the CB of Co_3O_4 to the ITO electrode, inhibiting the rapid recombination of photogenerated electron–hole pairs.

Inspired by these studies, Ryu's research group further conducted a comprehensive investigation of POM NCs as primary building blocks for fabricating spatially multilayered photoanodes. As shown in Fig. 8c, a LbL assembly strategy was employed to deposit various cationic polyelectrolytes including BPEI, PDDA, PAH, or linear-poly(ethylenimine) (l-PEI), along with tetracobalt-substituted polyoxometalate $[Co_4(H_2O)_2(PW_9O_{34})_2]^{10-}$ (Co-POM) on different metal oxide substrates (Fe_2O_3, $BiVO_4$, TiO_2).[107] Interestingly, regardless of the type of PE used, the Fe_2O_3/(PE/Co-POM)$_n$ photoanodes exhibit significant PEC performance improvement compared with bare Fe_2O_3. This is attributed to the alternating cationic and anionic material layers formed by LbL assembly, which function as interfacial dipoles and help reduce charge transfer resistance. Furthermore, when the same deposition was applied to $BiVO_4$ and TiO_2 substrates, the resulting photoanodes show notable enhancements in both stability and PEC performances. To further demonstrate the advantages of the LbL assembly, a randomly mixed film compromising b-PEI and POM was prepared on Fe_2O_3 *via* a drop-casting method. However, compared with the LbL-assembled Fe_2O_3/(b-PEI/Co-POM)$_{10}$ multilayer heterostructure photoanode, it exhibits negligible photocurrent density. This indicates that well-defined interface structure and integration mode enabled by LbL assembly are crucial for

enhancing the PEC performances. Moreover, Choi *et al.* deposited positively charged graphene oxide (GO) and negatively charged Co-POM $[Co_4(H_2O)_2(PW_9O_{34})_2]^{10-}$ on Fe_2O_3 through LbL assembly technology.[108] The results demonstrate that compared with bare Fe_2O_3, the Fe_2O_3/(Co-POM/GO)$_n$ spatially multilayered photoanode exhibits significantly enhanced OER performance (Fig. 8d) while maintaining good stability during prolonged PEC reactions. This enhancement stems from GO serving as an efficient hole transport material and Co-POM acting as an effective water oxidation catalyst, with the tightly integrated multilayer film enabled by LbL assembly maximizing their synergistic effects on electron transfer. In another study, Kim *et al.* used a LbL assembly strategy to deposit Co-POM $[Co_4(H_2O)_2(PW_9O_{34})_2]^{10-}$ and l-PEI on $BiVO_4$, resulting in $BiVO_4$/(l-PEI/Co-POM)$_n$ multilayer photoanodes, while nickel-containing POM $[Ni_4(H_2O)_2(VW_9O_{34})_2]^{10-}$ (Ni-POM) and PEI were assembled on the Cu_2O, forming the Cu_2O/(l-PEI/Ni-POM)$_n$ photocathodes.[109] The results revealed that the PEC cell achieved unassisted water splitting under zero external bias, with its photocurrent density demonstrating remarkable stability for at least 2 h (Fig. 8e and f). This significant enhancement can be attributed to: (1) improved charge transfer due to catalyst deposition; (2) enhanced charge transport to the catalyst through the formation of interfacial dipoles; (3) increased stability resulting from the protective coating formation. Another noteworthy aspect is that conventional functionalization methods for photoelectrodes are typically material-specific and require harsh processing conditions (*e.g.*, vacuum/high-temperature treatments) along with complex chemical syntheses, often involving toxic/hazardous chemicals (such as HF and H_2SO_4). In contrast, the LbL assembly strategy developed in this study enables the fabrication of PEC devices entirely utilizing aqueous building block solutions under ambient conditions, representing an environmentally benign approach. This simple, universally applicable, and eco-friendly methodology demonstrates significant practical value for real-world applications. Therefore, the deposition of highly catalytically active POMs using LbL assembly technology demonstrates definitive and universal significance for enhancing the PEC performance of MOs. In particular, $[Co_4(H_2O)_2(PW_9O_{34})_2]^{10-}$ serves as an ideal building block that will provide guiding principles for the design of future multilayer spatial structures.

4.4. LbL assembly with nanoparticles as building blocks

4.4.1. Metal nanoparticles. Metal nanoparticles (MNPs), typically ranging in size from 1 to 100 nm, have garnered significant attention in photoelectrocatalysis due to their unique surface plasmon resonance (SPR) effect.[110] The SPR effect occurs when the collective oscillation frequency of free electrons on the surface of MNPs coincides with the frequency of incident photons, resulting in strong photon absorption at specific energies by the metallic material.[111] For instance, gold NPs (Au NPs) synthesized using the citrate reduction method with a diameter of 12 nm exhibit SPR absorption at 520 nm.[112] The integration of MNPs with semiconductors enhances the PEC water splitting efficiency through a triple synergistic mechanism: (1) MNPs effectively extend the light absorption range of semiconductors to the visible and even near-infrared spectrum domain; (2) the localized electromagnetic field induced by the SPR effect promotes the generation of electron–hole pairs within the semiconductor, significantly increasing the carrier generation rate; (3) hot electrons photoexcited by the SPR effect are injected into the CB of the semiconductor, directly participating in the HER.[113] For example, Cao *et al.* alternately deposited Au NPs and Au nanorods (NRs) onto TNRAs, with the UV-Vis absorption spectra showing the SPR effect of Au NPs at 530 nm and the longitudinal SPR effect of Au NRs at 680 nm.[114] Xiao *et al.* employed a LbL assembly strategy to uniformly load multilayer MNPs (M = Au, Ag, Pt) on TNTAs.[50] The unique SPR effect of MNPs significantly extends the lifetime of photogenerated electrons by enhancing charge separation. Meanwhile, MNPs serve as highly active catalytic centers, substantially boosting the PEC water oxidation performances. Building on this work, Xiao *et al.* further deposited Au NPs and Au_x NCs on TNTAs using an analogous LbL assembly technique.[115] The PL results indicate that Au NPs can modulate the lifetime of electron–hole pairs generated over Au_x NCs, while both Au_x NCs and Au NPs can effectively capture electrons from the oxygen vacancy energy levels of TiO_2, thereby promoting the charge separation of the photoanode. These effects originate from the favorable energy level alignment formed between Au_x NCs and TiO_2 as well as the intimate interface provided by LbL assembly, further enhancing the electron relay function of Au NPs as bridging mediators (Fig. 9a). Moreover, the TNTAs/Au NPs/Au_x NCs multilayer photoanode demonstrates excellent photostability under prolonged visible light irradiation, verifying the stable and reliable electrostatic interaction between building blocks in steering the LbL assembly construction. This work pioneers a novel strategy for rationally constructing semiconductor heterostructures co-modified by MNPs and MNCs, revealing the important role of Au NPs as an electron relay mediator and role of Au_x NCs as a plasmonic photosensitizer. In addition, MNPs can also function as Schottky junction electron traps. For example, Lin *et al.* fabricated a composite photoanode consisting of Au NPs and WO_3 NRs *via* LbL assembly.[56] The results indicated that Au NPs served as electron traps, improving the electron transfer dynamics of WO_3 and significantly enhancing its PEC water oxidation performances. In another case, Kim *et al.* employed a LbL assembly approach to deposit Ag NPs and Co-POM on the Fe_2O_3 substrate.[116] In this artificial PEC system, bare Fe_2O_3 exhibited a faradaic efficiency of merely 62%, whereas the Fe_2O_3/(Co-POM)$_{10}$/(Ag NPs)$_5$ photoanode achieved a remarkable efficiency of 97% (Fig. 9b). This enhancement is attributed to the role of Ag NPs as a photosensitizer that effectively extends the light absorption range of the Fe_2O_3 substrate (320–560 nm) with Co-POM functioning as a cocatalyst to significantly facilitate interfacial electron transfer. The Fe_2O_3/(Co-POM)$_{10}$/(Ag NPs)$_5$ multilayer heterostructure exhibits no obvious photocurrent decay for the 12 h PEC reaction, verifying its excellent stability endowed by LbL assembly. It is noteworthy that by varying the number of cyclic deposition cycles of Ag NPs, the PEC

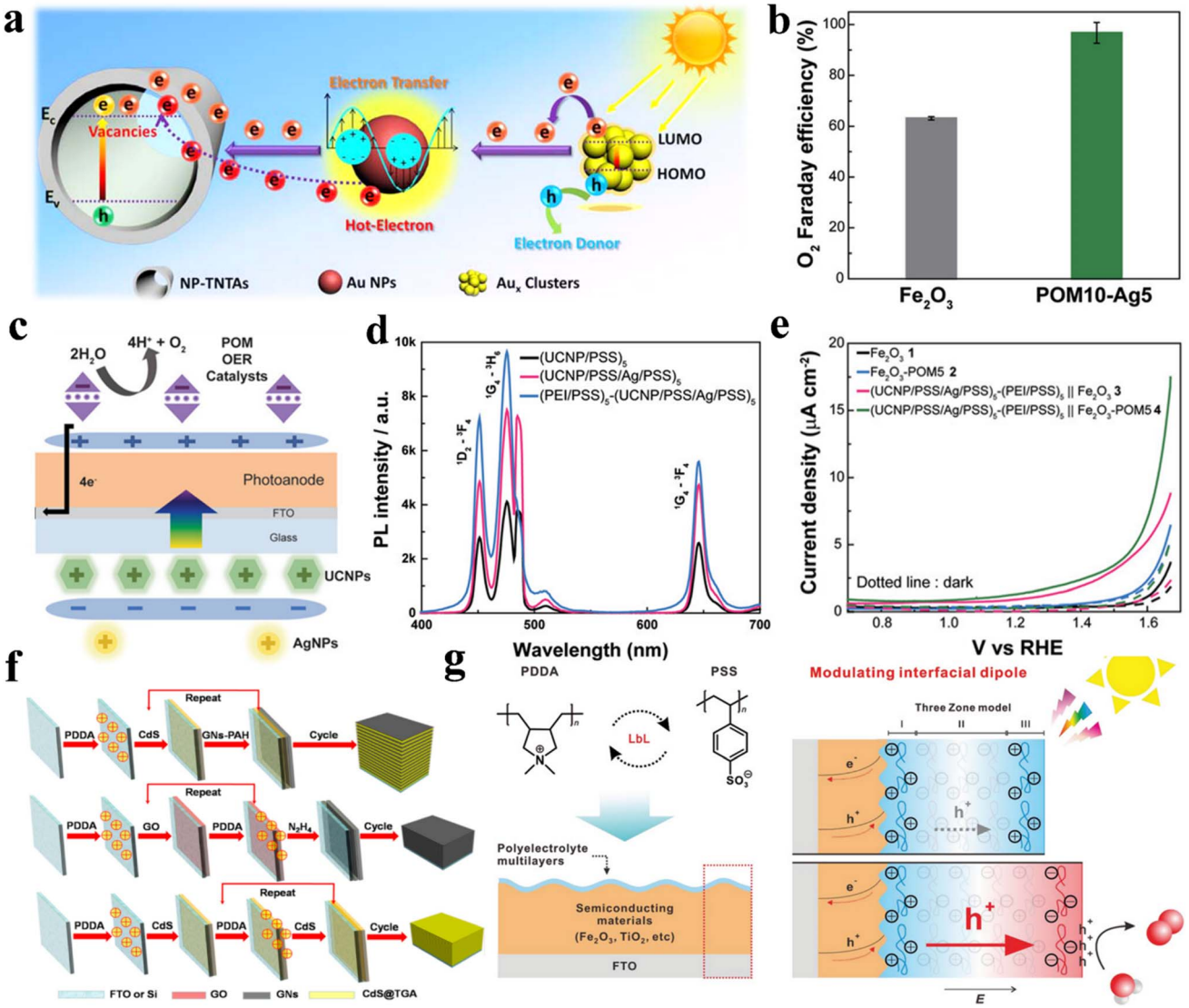

Fig. 9 (a) Schematic illustration of electron transfer pathways in TNTAs/Au NPs/Au$_x$ NCs multilayer nanostructured photoanodes (reprinted with permission from ref. 115, Copyright 2015 American Chemical Society). (b) Faradaic efficiency of Fe_2O_3/(Co-POM)$_{10}$/(Ag NPs)$_5$ photoanodes. (c) A diagram showing the LbL assembly of UCNPs, Ag NPs, and POM. (d) PL spectra of (UCNP/PSS/Ag/PSS)$_3$. (e) LSV curves of (Ag NPs/UCNPs)$_5$/Fe_2O_3/(Co-POM)$_5$ (reprinted with permission from ref. 116, Copyright 2019 Wiley-VCH Verlag). (f) Flowcharts for LbL assembly of GNs/CdS QDs, GNs, and CdS QDs multilayers (reprinted with permission from ref. 120, Copyright 2014 American Chemical Society). (g) Schematic illustration of LbL-assembled polyelectrolyte multilayers and charge carrier transport pathways during PEC water oxidation (reprinted with permission from ref. 121, Copyright 2019 Wiley-VCH Verlag).

performance of the multilayer structure was modulated. This observation is consistent with the theoretical principle that the plasmonic enhancement effect reaches its optimum when the separation distance between the plasmonic enhancer (*i.e.*, Ag NPs) and the light-harvesting components is on the order of several nanometers or angstroms. These results demonstrate the efficacy of the LbL assembly method for precisely assembling functional building blocks at the nanoscale.

4.4.2. Up-conversion nanoparticles. Up-conversion nanoparticles (UCNPs) are inorganic crystalline nanomaterials doped with lanthanide elements such as Y, Nd, Yb, Er, and Tm.[117] The unique anti-Stokes photoluminescence (PL) properties of UCNPs are manifested as follows: UCNPs absorb multiple low-energy near-infrared (NIR) photons, undergo energy transfer between lanthanide ions (*e.g.*, $Yb^{3+} \rightarrow Er^{3+}$ or $Yb^{3+} \rightarrow Tm^{3+}$), and ultimately emit higher-energy ultraviolet (UV) or visible photons through sequential multiple energy-level transitions.[118] Therefore, integration of UCNPs with a semiconductor can significantly enhance the NIR-light utilization efficiency of the semiconductor, thereby improving the PEC water splitting performances. For example, Lim *et al.* deposited core–shell–shell structured UCNPs ($NaYF_4$:Yb, Nd, Tm@$NaYF_4$:Yb, Nd@$NaYF_4$) and $ZnFe_2O_4$ sequentially on the TiO_2 nanorods.[119] Compared with pure UCNPs, the PL spectrum of the TiO_2/$ZnFe_2O_4$/UCNPs photoanodes under 980 nm light excitation showed a significant reduction in UV and blue-light

emission intensities, indicating effective energy transfer from UCNPs to TiO_2 and $ZnFe_2O_4$. Additionally, $TiO_2/ZnFe_2O_4$/UCNPs photoanodes exhibited the optimal ABPE (0.41%), confirming that the anti-Stokes PL properties of UCNPs effectively boost the PEC water oxidation performances of TiO_2. To further explore the potential of UCNPs, Kim *et al.* employed a LbL assembly strategy to deposit UCNPs ($NaYF_4$:Yb/Tm@$NaYF_4$), Ag NPs, and Co-POM onto Fe_2O_3 substrates.[116] As shown in Fig. 9c, Ag NPs and UCNPs are successively assembled on the back of FTO glass using negatively charged polyelectrolytes, while Co-POM is deposited on the Fe_2O_3 through positively charged polyelectrolytes. This assembly strategy effectively mitigates reaction site obstruction in PEC water splitting over Fe_2O_3 caused by multilayer films. The PL results demonstrate that the SPR effect of Ag NPs enhanced the blue emission of UCNPs at 480 nm by 180% (Fig. 9d). Meanwhile, the $(Ag\ NPs/UCNPs)_5/Fe_2O_3/(Co\text{-}POM)_5$ composite photoanodes exhibited superior PEC water splitting performances under 980 nm NIR irradiation (Fig. 9e), which is attributed to the up-conversion properties of UCNPs and the synergistic interactions among the different building blocks. This study conclusively illustrates that the LbL assembly technique provides an efficient and straightforward approach to precisely control functional building blocks at the nanoscale without compromising their inherent properties. This innovative assembly method provides valuable insights and strategies for the fabrication of advanced solar-to-chemical energy conversion devices.

4.5. LbL assembly with layered materials as building blocks

4.5.1. Graphene nanosheets. 2D graphene nanosheets (GNs) have been widely utilized to prepare efficient photoelectrodes owing to their excellent light absorption, large specific surface area, and high conductivity.[122] LbL assembly technology provides a technical pathway to maximize the advantages of 2D GNs. For example, Kavitha *et al.* employed a LbL assembly technique to deposit negatively charged reduced graphene oxide nanosheets (rGNs) and positively charged ZnO on an FTO substrate.[123] The results indicated that rGNs facilitated the effective separation of electron–hole pairs over ZnO, and this promoting effect strengthened with the increase in the assembly layer number. Teh *et al.* further investigated the effect of different assembly sequences of rGNs and ZnO on their PEC water oxidation performances.[124] The EIS results demonstrate that the assembly of rGO on the backside of ZnO reduces the charge transfer resistance of the semiconductor film, while the assembly of rGO on the front-side participates in the chemical water activation process. Furthermore, the capacitive behavior of ZnO weakens upon the incorporation of rGO, which is attributed to the formation of n–p heterojunctions between them that effectively suppress electron–hole recombination. Consequently, the rGO/ZnO multilayer nanocomposite constructed *via* LbL assembly features an intimately connected interface, wherein rGO serves as an electron acceptor, thereby accelerating the efficient migration of photogenerated charge carriers over ZnO. As shown in Fig. 9g, Xiao *et al.* employed an electrostatic LbL assembly approach to PAH modified GNs and TMC QDs (CdS, CdSe, CdTe) on an FTO substrate.[120] Compared with pure $(CdS\ QD)_{15}$ and $(GNs)_{15}$ photoanodes, the $(GNs/CdS\ QD)_{15}$ photoanode exhibited optimal PEC water splitting performances. This enhancement effect originates from the intimate alternating integration between CdS QDs and GNs, which maximizes the structural advantages of two-dimensional GNs in the GNs/CdS QD composite film, ultimately optimizing charge separation and transport within the composite film. Moreover, the favorable energy level alignment between GNs and CdS QDs provides the fundamental basis for the rapid directional transfer of photogenerated electrons from CdS QDs to GNs. Kim *et al.* developed a LbL assembly technique to load GNs and a ruthenium-terpyridine coordination complex (TPY_2Ru) on the ITO substrate, resulting in bifunctional photoelectrode $(TPY_2Ru/GNs)_n$ that can function as both a photoanode and photocathode.[125] The photoelectrode achieved a maximum photoanodic current density of 4.28 μA cm^{-2} (1.23 V *vs.* RHE) and a maximum photocathodic current density of 28.42 μA cm^{-2} (0 V *vs.* RHE), representing significant enhancement compared with single component electrodes. This improvement originates from TPY_2Ru generating photoinduced excitons while GNs suppress charge carrier recombination in the electrode, thereby further promoting photogenerated electron transfer. Moreover, the LbL assembly creates intimate interfacial contact between TPY_2Ru and GNs, with the abundant defects accumulated at the interface facilitating the formation of an effective Z-scheme structure that additionally accelerates directional electron transfer. Remarkably, the $(TPY_2Ru/GNs)_n$ multilayer photoelectrode maintain 100% and 96% retention of photocurrent density for the OER and HER, respectively, after 1000 bending durability test cycles at a curvature radius of 6.0 mm. This outstanding mechanical flexibility is a result of not only the soft material property but also the versatile LbL method enabling conformal deposition on any uneven substrate and assembling various nanomaterials at a molecular level into the hybrid multilayer films. Thus, these results demonstrate that the molecularly assembled LbL photocatalytic electrode can be applied in PEC water splitting and flexible optoelectronic devices, which is challenging for conventional inorganic electrodes. This strategy of assembling organic photoactive materials and inorganic nanomaterials provides valuable insights for the future fabrication of novel photoelectrodes.

4.5.2. Polyelectrolyte multilayer films. Polyelectrolytes are long-chain polymers with ionizable groups that exhibit unique charge modulation and interface optimization properties, offering significant advantages in the fabrication of photoelectrodes.[126] For example, Bian *et al.* deposited novel carbazole organic molecules (CS-38) and nickel(II) phthalocyanine-tetrasulfonic acid tetrasodium salt (TsNiPc) sequentially on the ITO substrate.[127] The CS-38/TsNiPc multilayer film photoanodes exhibited excellent PEC water splitting performances, attributed to the roles of CS-38 as both an organic photosensitizer and hole transfer mediator, while the integration of CS-38 and TsNiPc films further improved the OER kinetics. For example, Liu *et al.* developed a LbL assembly technique to uniformly deposit a non-conjugated polymer of PDDA on the

TNRAs.[128] Compared with pure TNRA photoanodes, the LbL-assembled TNRAs-$(PDDA)_4$ photoanodes exhibited markedly enhanced PEC water oxidation performances under simulated sunlight irradiation. This improvement is attributed to the crucial role of the positively charged quaternary ammonium functional group in PDDA, which effectively captures photogenerated electrons from TiO_2, thereby significantly promoting electron–hole pair separation in TiO_2. Similarly, Yuan *et al.* utilized an analogous LbL assembly strategy to periodically deposit a polyelectrolyte of PAH on metal oxide (MO: WO_3, ZnO, TiO_2) substrates.[129] Compared with pristine MO photoanodes, the MOs-$(PAH)_4$ photoanodes demonstrated higher charge injection and separation efficiency. This is attributed to the crucial role of amine functional groups in PAH that benefits hole capture, effectively suppressing the electron–hole pair recombination over MOs. In another exemplary case involving multilayer polyelectrolytes, Choi *et al.* conducted comprehensive investigations into the interfacial charge transfer resistance of Fe_2O_3/(l-PEI/PAA)$_3$ photoanodes.[108] Their work establishes that interfacial dipole moment generated between the polyelectrolyte layers effectively modulates the flat-band potential of Fe_2O_3 while optimizing its band alignment, thereby creating more thermodynamically favorable conditions for the overall water splitting reaction. Additionally, as shown in Fig. 9h, Ryu *et al.* employed a LbL assembly approach to load cationic PDDA and anionic poly(styrene sulfonate) on Fe_2O_3 substrates.[121] The results showed that after loading the multilayer films, the photocurrent density of the Fe_2O_3 photoanodes increased from 0.32 to 0.41 mA cm^{-2} (1.6 V *vs.* RHE). This is attributed to the interfacial dipole layer formed by the multilayer polyelectrolytes, which causes the vacuum energy level near the photoelectrode–electrolyte interface to bend upward, thereby providing a greater thermodynamic driving force for efficient carrier separation. Importantly, the magnitude and direction of the interfacial dipole moment at the photoelectrode interface can be tuned by controlling the number and type of polyelectrolytes, further enhancing charge separation efficiency. Building on this, Ryu *et al.* further loaded Co-POM onto a Fe_2O_3/(PDDA/PSS)$_3$/(PDDA/POM)$_3$ photoanode, achieving an even higher photocurrent density. This improvement is due to the significantly enhanced charge separation efficiency in the presence of the interfacial dipole layer, along with the dramatically increased charge injection efficiency enabled by the POM catalyst. Therefore, considering the crucial role of polyelectrolyte layers with specific functions in charge transfer, this ideal building block model will inspire new ideas for the ingenious design of spatially multilayered structures in the future.

5. Structure–performance mechanism analysis

In recent years, significant progress has been made in fabricating spatially multilayered heterostructure photoelectrodes by integrating diverse functional building blocks using the LbL assembly technique. However, due to the wide scope of building blocks and the lack of precise characterization tools, the structure–performance mechanism underlying LbL-assembled PEC devices remains unclear. In this section, we summarize the several classic models of functional building blocks (*e.g.*, TMC QDs, Ag NCs, and Au NCs) combined with metal oxides (MOs) to construct the multilayer heterostructure photoelectrodes. We further elucidate the correlation between the cascade charge transfer pathways enabled by these multilayer structures and their PEC performances. From the perspective of band structure, applicable energy level alignment between the building blocks and semiconductor substrate is fundamental to optimizing charge migration and separation. As shown in Fig. 10a, the energy level alignment between CdX QDs (X = Se, Te, S) modified with different ligands [2-aminoethanethiol (AET) and mercaptoacetic acid (MAA)] and the classical n-type semiconductor TiO_2 illustrates this optimization.[78] In such a carrier transfer model, photoexcited electrons are transferred from the CB of CdX QDs to the CB of TiO_2, participating in the reduction reaction. Similarly, in the multilayer heterostructure photoelectrode constructed with Ag NCs or Au NCs, photoexcited electrons migrate from the LUMO of metal NCs to the CB of TiO_2 (Fig. 10b and c).[90b,130]

On the other hand, it is important to note that polyelectrolyte (PE) thin films are a critical component in constructing multilayer heterostructure photoelectrodes, as exemplified by the classic MOs/(PE/metal NCs)$_n$ photosystems. During the LbL assembly process, PE thin films provide a strong electrostatic force to stabilize the integration of functional building blocks with different charge properties. Furthermore, the critical role of PE interlayers in facilitating charge transfer within multilayer architectures has been experimentally demonstrated. For example, the WO_3/$(PDDA)_2$ photoanode shows significantly enhanced photocurrent compared with WO_3/SiO_2/$(PDDA)_2$ with an interim insulating layer, highlighting the crucial role of PDDA in accelerating interfacial charge transfer.[23] In summary, the key roles of PE in LbL-assembled multilayer photoelectrodes are as follows: (1) acting as electrostatic adhesives for combining functional building blocks with opposite charge properties, (2) serving as an essential medium to improve charge migration and separation between the semiconductor substrate and functional building blocks, (3) forming interfacial dipoles that improve the flat-band potential of photoanodes and create more favorable thermodynamic conditions for water splitting reactions, and (4) functioning as an effective protective coating to reduce corrosion of multilayer photoelectrodes. Therefore, with modulating the favorable energy level alignment and harnessing the critical roles of PEs, coupled with the face-to-face intimate integration interface enabled by LbL assembly, a directional charge transfer mechanism is stimulated that significantly enhanced the charge transport and separation efficiency.

As illustrated in Fig. 10d and e, schematic diagrams depicting the cascade charge transfer mechanisms of MOs/(PDDA/Au_x NCs)$_n$ and TiO_2/(PDDA/MQDs)$_n$ multilayer heterostructure photoanodes are presented.[23,24] Specifically, in the MOs/(PDDA/Au_x NCs)$_n$ multilayer heterostructure, ultrathin PDDA layers are alternately and tightly intercalated at the interface of functional building block layers, acting as an efficient electron transfer

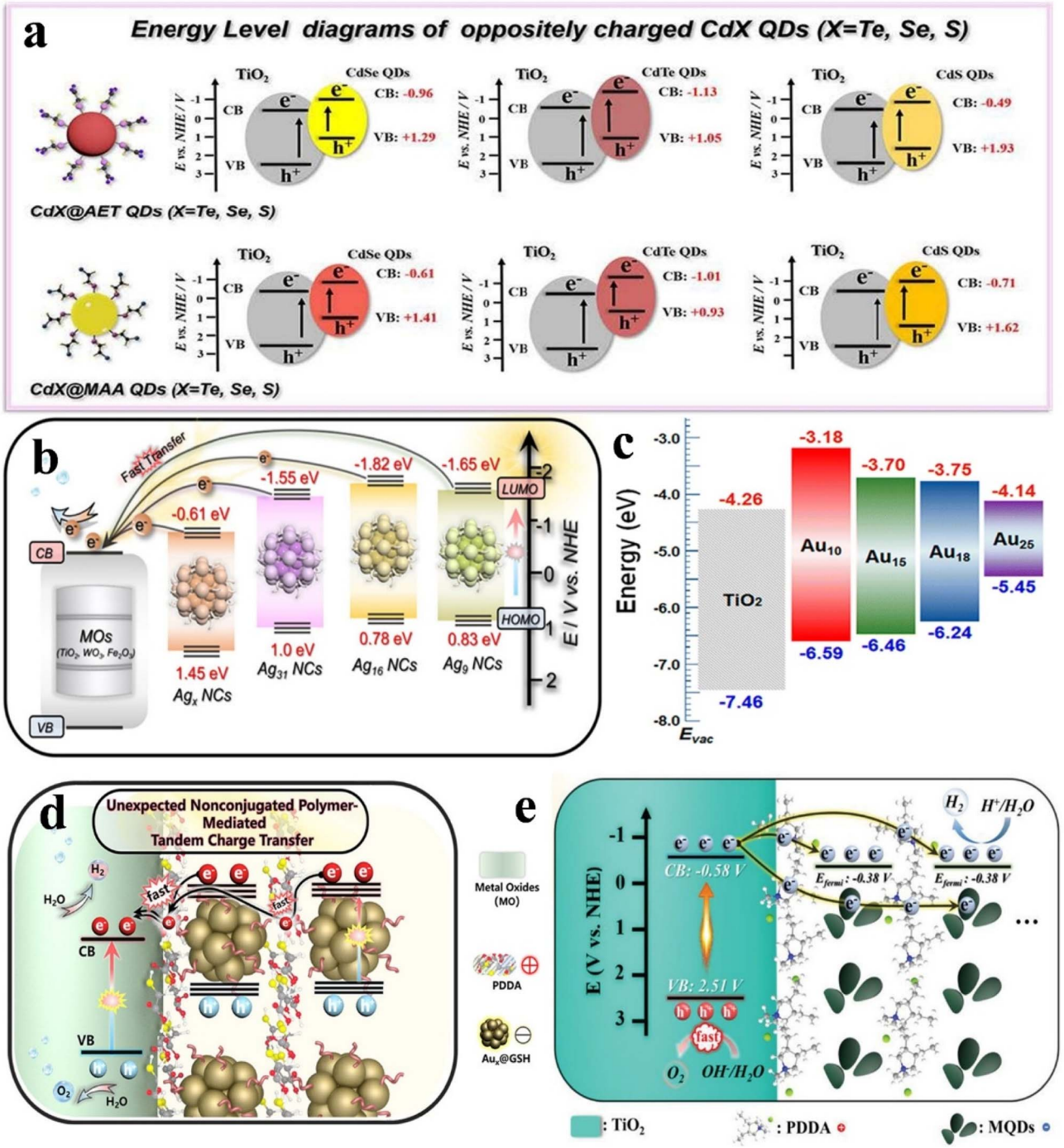

Fig. 10 (a) Schematic diagram of energy level matching between different CdX QDs (X = Se, Te, S) capped with AET and MAA ligands and TiO_2 (reprinted with permission from ref. 78, Copyright 2021 American Chemical Society). (b) Schematic diagram of energy level matching between different Ag NCs and TiO_2 (reprinted with permission from ref. 130, Copyright 2023 American Chemical Society). (c) Schematic diagram of energy level matching between different Au NCs and TiO_2 (reprinted with permission from ref. 90b, Copyright 2023 Royal Society of Chemistry). (d) Schematic illustration of the tandem charge transfer pathway of MOs/(PDDA/Au_x NCs)$_n$ heterostructures (reprinted with permission from ref. 23, Copyright 2021 American Chemical Society). (e) Schematic diagram depicting the charge transport characteristic of TiO_2/(PDDA/MQDs)$_n$ photoanodes (reprinted with permission from ref. 24, Copyright 2023 Wiley-VCH Verlag).

mediator. Therefore, the non-conjugated polymer of PDDA accelerates the unidirectional electron transfer from the adjacent Au_x NC layer to the CB of MOs (WO_3, TiO_2, Fe_2O_3). Through this configuration design, the spatially stacked ultrathin PDDA layers serve as relays for cascade electron transfer, effectively suppressing the charge recombination over Au_x NCs. Hence, the synergistic interaction of the alternately deposited ultrathin PDDA layer and Au_x@GSH NCs endowed by LbL assembly as

a charge transfer mediator and light harvesting antennae for constructing tandem charge transfer channel leads to the substantially enhanced PEC water oxidation activities of MOs/$(PDDA/Au_x)_2$ heterostructures under simulated solar and visible light irradiation. Moreover, extensive experimental evidence demonstrates that this cascade charge transfer pathway is universally applicable to a wide variety of building blocks and substrate materials. Therefore, spatially multilayer photoelectrodes with cascade charge transfer pathways fabricated *via* the LbL assembly strategy provide critical paradigms for the future design of functionalized high-performance PEC devices.

6. Outlook and perspectives

The LbL assembly technique has become a widely adopted strategy for constructing spatially multilayer heterostructure photoelectrodes with an optimized charge transfer pathway, owing to its precise control over interfacial structure at the atomic scale. While the LbL assembly technique exhibits remarkable potential for constructing efficient PEC water splitting systems, significant challenges remain in the rational integration of advanced building blocks at the microstructural level to further improve STH conversion efficiency, which includes the following aspects:

(1) Structural stability under complex conditions: the long-term operational efficiency and durability of multilayered nanostructured photoelectrodes fabricated by LbL assembly, especially under intense light irradiation and in harsh aqueous environments, have not yet been fully achieved. Currently, functional layers are primarily connected by simple electrostatic interactions, which are not enough to maintain long-term structural stability. Future research should focus on the development of PEC devices incorporating stronger intermolecular interactions. For example, rational design of multilayer nanostructures supported by a combination of molecular interactions (*e.g.*, electrostatic forces, hydrogen bonds, covalent bonds, and biospecific interactions) could fundamentally enhance the stability between the functional layers. Moreover, integrating LbL assembly technology with scalable manufacturing techniques such as photolithography, inkjet printing, or 3D printing, while maintaining its inherent flexibility and precision, could significantly accelerate the design and development of next-generation PEC devices.

(2) Advanced functional building blocks: the exploration of novel materials remains a primary driving force for improving the PEC water splitting performance. Although this review summarizes several photosensitizers and co-catalysts used in LbL assembly, many promising candidate materials in the PEC field remain underexplored. For instance, perovskite materials with high photoelectric conversion efficiency, biomimetic catalysts with superior light-harvesting properties, and single-atom catalysts with exceptional catalytic activity possess significant potential for further development. It is anticipated that scientific integration of these powerful building blocks *via* the LbL assembly strategy could enable unprecedented STH conversion efficiencies.

(3) Mechanistic elucidation of LbL-assembled PEC devices and PEC reaction: due to the limitations of conventional characterization tools, the current understanding of the growth process and PEC water splitting reaction mechanism of LbL-assembled multilayer nanostructures is mainly at the theoretical level. Specifically, multilayer thin-film photoelectrodes prepared from ultrathin polyelectrolytes possess an ultralow deposition amount, making it challenging to directly observe their internal structures using conventional characterization tools such as SEM, TEM, or atomic force microscopy (AFM). Utilizing more advanced characterization techniques like aberration-corrected transmission electron microscopy (AC-TEM), *in situ* TEM, and focused ion beam scanning electron microscopy (FIB-SEM) is crucial for confirming the integrated architectures of various functional building blocks. Moreover, unraveling the rapid and complex charge separation and transfer process in PEC water splitting reactions is critical for improving the STH conversion efficiency of PEC devices. In the future, more advanced *in situ* characterization methods such as transient absorption spectroscopy (TAS), ambient pressure X-ray photoelectron spectroscopy (AP-XPS), and secondary ion mass spectrometry (SIMS) can provide deeper insights into these unexplored processes. In addition, introduction of theoretical computational models in LbL-assembled multilayer heterostructures will provide valuable insights into the interaction between different building blocks. For example, Yu *et al.* employed first principles density functional theory (DFT) to investigate the binding modes between different components in LbL-assembled multilayer structures.[131] Specifically, the Multiwfn software based on efficient algorithms can be used to evaluate the strength of electrostatic interaction in diverse binding configurations, while VMD (Visual Molecular Dynamics) can generate color-coded van der Waals surface diagrams of various binding modes and calculate their corresponding binding energies, visually demonstrating the steric effects. By constructing theoretical models of different building block materials, parameters such as binding energies, charge densities, oxygen vacancies, and free energy changes can be computed, thereby providing more definitive explanations for reaction mechanisms.[132] These computational models establish a rigorous theoretical framework for elucidating interfacial interaction in LbL-assembled systems, whose deeper implementation should be prioritized in future studies.

(4) Intelligent AI design: the integration of artificial intelligence (AI) and machine learning technologies into LbL assembly and PEC reactions undoubtedly represents a critical future research direction. By leveraging AI algorithms, researchers can rapidly screen potential high-performance building block materials based on existing data such as physicochemical properties, energy level alignment, and interfacial interaction.[133] For instance, combining high-throughput computational and experimental databases, AI can predict optimal material combinations and assembly strategies, thereby significantly reducing experimental exploration time and costs. Furthermore, deep learning techniques can analyze how various parameters including deposition sequence, duration, and concentration influence the final PEC performances,

establishing the comprehensive parameter-performance mapping models. Additionally, AI-based predictive models can forecast performance degradation in multilayer photoelectrodes during prolonged operation, identifying key failure mechanisms such as material decomposition or building block deactivation and proposing targeted optimization strategies.[134] Following this developmental roadmap, future AI-embedded LbL and PEC systems will achieve fully automated deposition control and intelligent experimental analysis through real-time data acquisition and processing, ultimately advancing intelligent, modular, and highly efficient operation.

However, this intelligent transformation faces significant challenges. For example, the LbL assembly process involves diverse materials and complex interfacial interactions, yet currently available high-quality data such as precise energy level alignment and intermolecular forces remain limited, constraining AI model accuracy. Addressing this requires collaborative efforts to generate large-scale, high-precision databases through high-throughput experimental platforms and advanced *in situ* characterization techniques such as *in situ* XPS and Raman spectroscopy. Moreover, designing multilayer photoelectrodes for PEC applications involves intricate physicochemical processes that current AI models struggle to fundamentally comprehend and explain. Developing AI algorithms that intrinsically incorporate physicochemical principles while integrating empirical data from techniques like Kelvin probe force microscopy and EIS may provide deeper mechanistic insights.[135] Most crucially, realizing this vision demands sophisticated hardware support, including precision sensors, real-time data acquisition systems, and high-speed computing capabilities, all of which will undoubtedly mature alongside advancements in computing and energy technologies. Therefore, establishing comprehensive databases to support reliable benchmark AI models has emerged as an urgent priority, necessitating coordinated efforts across the global LbL research community.

7. Conclusions

In summary, this work comprehensively summarized the latest developments of PEC water oxidation mediated by LbL assembly. The principles of LbL assembly and PEC water splitting are concisely introduced, and then a large variety of spatially multilayer heterostructure photoelectrodes fabricated by LbL assembly are elucidated, followed by a presentation of the emerging vision in this booming research field. The present review will provide fresh insights and practical guidance for the strategic design of advanced PEC devices *via* the LbL assembly strategy, thereby offering strong technical support for the large-scale development of green hydrogen energy in the future.

Author contributions

Wen-Cheng Liu and Yan-Qing Cai drafted the manuscript. Fang-Xing Xiao guided this work and corrected the manuscript. All the authors contributed to a critical discussion on the data and the manuscript.

Conflicts of interest

The authors declare no conflict of interest.

Abbreviations

LbL	Layer-by-layer
STH	Solar-to-hydrogen
PEC	Photoelectrochemical
LB	Langmuir Blodgett
SAMs	Self-assembled monolayers
CVD	Chemical vapor deposition
0D	Zero-dimensional
2D	Two-dimensional
3D	Three-dimensional
TMC QDs	Transition metal chalcogenide quantum dots
GR	Graphene
GO	Graphene oxide
VB	Valence band
CB	Conduction band
RHE	Reversible hydrogen electrode
HER	Hydrogen evolution reaction
OER	Oxygen evolution reaction
LSV	Linear sweep voltammetry
OCVD	Open-circuit photovoltage decay
ABPE	Applied bias photon-to-current efficiency
IPCE	Incident photon-to-current conversion efficiency
FE	Faradaic efficiency
PL	Photoluminescence
SEM	Scanning electron microscopy
TEM	Transmission electron microscopy
AFM	Atomic force microscopy
PSS	Poly(4-styrenesulfonic acid)
FTO	Fluorine-doped tin oxide
ITO	Indium tin oxide
NPAs	Nanoplate arrays
NRs	Nanorods
MOs	Metal oxides
TNRAs	TiO_2 nanorods
MOF	Metal–organic framework
TNTAs	TiO_2 nanotube arrays
GSH	L-Glutathione
PDDA	Poly(diallyl-dimethylammonium chloride)
BPEI	Branched poly-ethyleneimine
l-PEI	linear-poly(ethylenimine)
TNBs	TiO_2 nanobelts
NPs	Nanoparticles
NWs	Nanowires
N-GQDs	Nitrogen-doped graphene quantum dots
PAH	Poly(allylamine hydrochloride)
QDs	Quantum dots
AET	2-Aminoethanethiol
MAA	Mercaptoacetic acid
NCs	Nanocrystals
MNCs	Metal nanoclusters
POMs	Polyoxometalates
MNPs	Metal nanoparticles
SPR	Surface plasmon resonance

UCNPs	Up-conversion nanoparticles
NIR	Near-infrared
GNs	Graphene nanosheets
rGO	Reduced graphene oxide
AI	Artificial intelligence

Data availability

No primary research results, software or code have been included and no new data were generated or analysed as part of this review.

Acknowledgements

The support by the award Program for Minjiang scholar professorship is gratefully acknowledged. This work was financially supported by the National Natural Science Foundation of China (No. 21703038, 22072025) and Fujian Institute of Research on the Structure of Matter, Chinese Academy of Science acknowledged (No. 20240018).

References

1 T. Hisatomi, J. Kubota and K. Domen, *Chem. Soc. Rev.*, 2014, **43**, 7520–7535.
2 H. Wu, H. L. Tan, C. Y. Toe, J. Scott, L. Z. Wang, R. Amal and Y. H. Ng, *Adv. Mater.*, 2019, **32**, 1904717.
3 (*a*) W. Chen, D. H. Wang, W. Y. Wang, X. Liu, Y. Y. Liu, C. Wang, Y. Kang, S. Fang, X. D. Yang, W. G. Gu, D. Y. Luo, Y. M. Luo, Z. T. Qu, C. J. Zuo, Y. Kang, L. Cheng, W. S. Yan, W. Hu, R. Long, J. H. He, K. Liang, S. Liu, Y. J. Xiong and H. D. Sun, *Nat. Commun.*, 2025, **16**, 879; (*b*) J. W. Ager, M. R. Shaner, K. A. Walczak, I. D. Sharp and S. Ardo, *Energy Environ. Sci.*, 2015, **8**, 2811–2824.
4 F. Safari and I. Dincer, *Energy Convers. Manage.*, 2020, **205**, 112182.
5 B. Alfakes, C. Garlisi, J. Villegas, A. Al-Hagri, S. Tamalampudi, N. S. Rajput, J. Y. Lu, E. Lewin, J. Sá, I. Almansouri, G. Palmisano and M. Chiesa, *Surf. Coat. Technol.*, 2020, **385**, 125352.
6 C. H. Kwon, Y. Ko, D. Shin, M. Kwon, J. Park, W. K. Bae, S. W. Lee and J. Cho, *Nat. Commun.*, 2018, **9**, 4479.
7 (*a*) A. Wichmann, G. Schnurpfeil, J. Backenköhler, L. Kolke, V. A. Azov, D. Wöhrle, M. Bäumer and A. Wittstock, *Tetrahedron*, 2014, **70**, 6127–6133; (*b*) Y. Paz, *Beilstein J. Nanotechnol.*, 2011, **2**, 845–861.
8 B. J. Liu, Q. Chen, Q. L. Mo and F. X. Xiao, *Coord. Chem. Rev.*, 2023, **493**, 215285.
9 J. F. Quinn, A. P. R. Johnston, G. K. Such, A. N. Zelikin and F. Caruso, *Chem. Soc. Rev.*, 2007, **36**, 707–718.
10 J. J. Richardson, M. Björnmalm and F. Caruso, *Science*, 2015, **348**, 2491.
11 F. X. Xiao, M. Pagliaro, Y. J. Xu and B. Liu, *Chem. Soc. Rev.*, 2016, **45**, 3088–3121.
12 R. K. Iler, *J. Colloid Interface Sci.*, 1966, **21**, 569–594.
13 G. Decher, J. D. Hong and J. Schmitt, *Thin Solid Films*, 1992, **210**, 831–835.
14 B. Y. Ning, S. H. He, X. Lin and F. X. Xiao, *Inorg. Chem.*, 2024, **63**, 23742–23748.
15 I. M. Thomas, *Appl. Opt.*, 1987, **26**, 4688–4691.
16 J. J. Richardson, J. Cui, M. Björnmalm, J. A. Braunger, H. Ejima and F. Caruso, *Chem. Rev.*, 2016, **116**, 14828–14867.
17 S. Dey, K. Mohanta and A. J. Pal, *Langmuir*, 2010, **26**, 9627–9631.
18 Y. J. Zhang, S. G. Yang, Y. Guan, W. X. Cao and J. Xu, *Macromolecules*, 2003, **36**, 4238–4240.
19 G. Decher, *Science*, 1997, **277**, 1232–1237.
20 S. Srivastava and N. A. Kotov, *Acc. Chem. Res.*, 2008, **41**, 1831–1841.
21 S. Hou, M. H. Huang, Y. B. Li, S. Xu, X. Lin, X. Y. Fu and F. X. Xiao, *Inorg. Chem.*, 2020, **59**, 16654–16664.
22 (*a*) S. T. Dubas, T. R. Farhat and J. B. Schlenoff, *J. Am. Chem. Soc.*, 2001, **123**, 5368–5369; (*b*) P. Bieker and M. Schönhoff, *Macromolecules*, 2010, **43**, 5052–5059.
23 Z. Q. Wei, S. Hou, X. Lin, S. Xu, X. C. Dai, Y. H. Li, J. Y. Li, F. X. Xiao and Y. J. Xu, *J. Am. Chem. Soc.*, 2020, **142**, 21899–21912.
24 S. Li, Q. L. Mo, S. C. Zhu, Z. Q. Wei, B. Tang, B. J. Liu, H. Liang, Y. Xiao, G. Wu, X. Z. Ge and F. X. Xiao, *Adv. Funct. Mater.*, 2022, **32**, 2110848.
25 B. J. Starr, V. V. Tarabara, M. Herrera-Robledo, M. Zhou, S. Roualdès and A. Ayral, *J. Membr. Sci.*, 2016, **514**, 340–349.
26 S. C. Zhang, M. Xing and B. Y. Li, *Int. J. Mol. Sci.*, 2018, **19**, 1641.
27 S. Li, Q. L. Mo, Y. Xiao and F. X. Xiao, *Coord. Chem. Rev.*, 2023, **477**, 214948.
28 A. E. Becquerel, *C. R. Acad. Sci.*, 1839, **9**, 145–149.
29 A. Fujishima and K. Honda, *Nature*, 1972, **238**(5358), 37–38.
30 J. Lin, W. Wang and G. Li, *Adv. Funct. Mater.*, 2020, **30**, 2005677.
31 I. Roger, M. A. Shipman and M. D. Symes, *Nat. Rev. Chem.*, 2017, **1**, 0003.
32 C. M. Ding, J. Y. Shi, Z. L. Wang and C. Li, *ACS Catal.*, 2017, **7**, 675–688.
33 L. Y. Yang, F. Li and Q. J. Xiang, *Mater. Horiz.*, 2024, **11**, 1638–1657.
34 S. Hou, H. W. Xie and F. X. Xiao, *Inorg. Chem.*, 2024, **63**, 8970–8976.
35 C. R. Jiang, S. J. Moniz, A. Q. Wang, T. Zhang and J. W. Tang, *Chem. Soc. Rev.*, 2017, **46**, 4645–4660.
36 C. Ding, J. Shi, Z. Wang and C. Li, *ACS Catal.*, 2017, **7**, 675–688.
37 H. J. Huang, D. S. Yu, F. Hu, S. C. Huang, J. N. Song, H. Y. Chen, L. L. Li and S. J. Peng, *Angew. Chem., Int. Ed.*, 2022, **61**, e202116068.
38 Y. Yoon, B. Yan and Y. Surendranath, *J. Am. Chem. Soc.*, 2018, **140**, 2397–2400.
39 B. A. Pinaud, J. D. Benck, L. C. Seitz, A. J. Forman, Z. Chen, T. G. Deutsch, B. D. James, K. N. Baum, G. N. Baum, S. Ardo, H. Wang, E. Miller and T. F. Jaramillo, *Energy Environ. Sci.*, 2013, **6**, 1983–2002.

40 K. Maeda and K. Domen, *J. Phys. Chem. Lett.*, 2010, **1**, 2655–2661.
41 M. G. Walter, E. L. Warren, J. R. McKone, S. W. Boettcher, Q. Mi, E. A. Santori and N. S. Lewis, *Chem. Rev.*, 2010, **110**, 6446–6473.
42 S. Kment, F. Riboni, S. Pausova, L. Wang, L. Wang, H. Han, Z. Hubicka, J. Krysa, P. Schmuki and R. Zboril, *Chem. Soc. Rev.*, 2017, **46**, 3716–3769.
43 J. T. Li and N. Q. Wu, *Catal. Sci. Technol.*, 2015, **5**, 1360–1384.
44 X. Yan, J. N. Yuan, F. X. Xiao and B. Liu, *Mater. Horiz.*, 2024, **11**, 5136–5140.
45 X. Zhang, Y. Liu, S. T. Lee, S. Yang and Z. Kang, *Energy Environ. Sci.*, 2014, **7**, 1409–1419.
46 H. Yang, J. Bright, S. Kasani, P. Zheng, T. Musho, B. Chen, L. Huang and N. Wu, *Nano Res.*, 2019, **12**, 643–650.
47 B. Tang, S. C. Zhu, H. Liang, S. Li, B. J. Liu and F. X. Xiao, *J. Mater. Chem. A*, 2022, **10**, 4032.
48 S. Hou, X. C. Dai, Y. B. Li, M. H. Huang, T. Li, Z. Q. Wei, Y. He, G. Xiao and F. X. Xiao, *J. Mater. Chem. A*, 2019, **7**, 22487.
49 Z. Y. Li, Y. H. Chen, J. R. Zhu, Q. Chen, S. J. Lu and F. X. Xiao, *Inorg. Chem.*, 2023, **62**, 16965–16973.
50 F. X. Xiao, *Chem. Commun.*, 2012, **48**, 6538–6540.
51 J. Y. Zhang and F. X. Xiao, *J. Mater. Chem. A*, 2017, **5**, 23681–23693.
52 C. C. L. McCrory, S. Jung, I. M. Ferrer, S. M. Chatman, J. C. Peters and T. F. Jaramillo, *J. Am. Chem. Soc.*, 2015, **137**, 4347–4357.
53 S. Gonçalves, P. Quitério, J. Freitas, D. Ivanou, T. Lopes, A. Mendes, J. P. Araújo, C. T. Sousa and A. Apolinário, *ACS Appl. Mater. Interfaces*, 2024, **16**, 64389–64409.
54 Z. Q. Wei, S. Hou, S. C. Zhu, Y. Xiao, G. Wu and F. X. Xiao, *Adv. Funct. Mater.*, 2022, **32**, 2106338.
55 Z. Y. Li, M. Yuan and F. X. Xiao, *Small*, 2025, **21**, 2409513.
56 H. J. Lin, T. Li, M. H. Huang, X. C. Dai, Y. B. Li and F. X. Xiao, *J. Phys. Chem. C*, 2019, **123**, 28066–28080.
57 Z. P. Zeng, F. X. Xiao, X. C. Gui, R. Wang, B. Liu, Y. Tan and T. Thatt, *J. Mater. Chem. A*, 2016, **4**, 16383–16393.
58 Q. Chen, Y. Xiao and F. X. Xiao, *Inorg. Chem.*, 2024, **63**, 1471–1479.
59 K. J. Kim and Y. R. Park, *Appl. Phys. Lett.*, 2001, **78**, 475–477.
60 L. Zhang, Y. Huang, C. H. Dai, Q. M. Liang, P. Yang, H. H. Yang and J. H. Yan, *J. Electron. Mater.*, 2019, **48**, 1724–1729.
61 Y. Q. Sun, B. Xu, Q. Shen, L. F. Hang, D. D. Men, T. Zhang, H. L. Li, C. C. Li and Y. Li, *ACS Appl. Mater. Interfaces*, 2017, **9**, 31897–31906.
62 S. J. Yuan, J. K. Mu, R. Y. Mao, Y. G. Li, Q. H. Zhang and H. Z. Wang, *ACS Appl. Mater. Interfaces*, 2014, **6**, 5719–5725.
63 X. Yan, H. W. Xie, G. Wu and F. X. Xiao, *Chin. Chem. Lett.*, 2025, **36**, 110279.
64 X. Y. Zhong, Y. L. Li, H. W. Wu and R. S. Xie, *Mater. Sci. Eng., B*, 2023, **289**, 116278.
65 G. Wu, Q. L. Mo, Y. Xiao, K. Wang, X. Z. Ge, S. R. Xu, J. L. Li, Y. Q. Shao and F. X. Xiao, *Inorg. Chem.*, 2023, **62**, 520–529.
66 Y. Liang, T. Tsubota, L. P. Mooij and R. van de Krol, *J. Phys. Chem. C*, 2011, **115**, 17594–17598.
67 G. L. Chang, D. G. Wang, Y. Y. Zhang, A. Aldalbahi, L. H. Wang, Q. Li and K. Wang, *Nucl. Sci. Tech.*, 2016, **27**, 108.
68 Y. B. Li and F. X. Xiao, *Inorg. Chem.*, 2025, **64**, 3608–3615.
69 (*a*) L. Cheng, Q. Xiang, Y. Liao and H. Zhang, *Energy Environ. Sci.*, 2018, **11**, 1362–1391; (*b*) Q. Chen, X. Z. Ge, L. H. Yu and F. X. Xiao, *Inorg. Chem.*, 2023, **62**, 19358–19365.
70 (*a*) W. Q. Fan, Q. H. Zhang and Y. Wang, *Phys. Chem. Chem. Phys.*, 2013, **15**, 2632–2649; (*b*) P. Su, X. Yan and F. X. Xiao, *Chem. Sci.*, 2024, **15**, 14778–14790.
71 Y. B. Li, T. Li, X. C. Dai, M. H. Huang, S. Hou, X. Y. Fu, Z. Q. Wei, Y. He, G. Xiao and F. X. Xiao, *ACS Appl. Mater. Interfaces*, 2020, **12**, 4373.
72 Y. X. Chen, M. Cheng, C. Lai, Z. Wei, G. X. Zhang, L. Li, C. S. Tang, L. Du, G. F. Wang and H. D. Liu, *Small*, 2023, **19**, 2205902.
73 (*a*) Q. L. Mo, J. L. Li, S. R. Xu, K. Wang, X. Z. Ge, Y. Xiao, G. Wu and F. X. Xiao, *Adv. Funct. Mater.*, 2023, **33**, 2210332; (*b*) Q. Chen, Y. H. Chen, J. R. Zhu, Z. Y. Li and F. X. Xiao, *Adv. Funct. Mater.*, 2025, **35**, 2417139.
74 (*a*) X. Z. Ge, K. Wang, Q. L. Mo, Y. Xiao, J. L. Li, G. Wu, S. R. Xu and F. X. Xiao, *Catal. Sci. Technol.*, 2023, **13**, 479–489; (*b*) Q. L. Mo, S. R. Xu, J. L. Li, X. Q. Shi, Y. Wu and F. X. Xiao, *Small*, 2023, **19**, 2300804.
75 M. A. Lukowski, A. S. Daniel, F. Meng, A. Forticaux, L. Li and S. Jin, *J. Am. Chem. Soc.*, 2013, **135**, 10274–10277.
76 (*a*) S. C. Zhu and F. X. Xiao, *ACS Catal.*, 2023, **13**, 7269–7309; (*b*) X. Yan, K. Wang and F. X. Xiao, *Inorg. Chem.*, 2023, **62**, 17454–17463.
77 (*a*) X. Yan, X. Y. Fu and F. X. Xiao, *Adv. Funct. Mater.*, 2023, **33**, 2303737; (*b*) M. Yuan, X. Yan, J. N. Yuan, P. Su, Q. Chen and F. X. Xiao, *J. Catal.*, 2024, **437**, 115667.
78 S. Hou, Q. L. Mo, S. C. Zhu, S. Li, G. G. Xiao and F. X. Xiao, *Inorg. Chem.*, 2021, **61**, 1188–1194.
79 S. Hou, Z. Q. Wei, X. C. Dai, M. H. Huang and F. X. Xiao, *Inorg. Chem.*, 2020, **59**, 7325–7334.
80 Z. Q. Wei, X. C. Dai, S. Hou, Y. B. Li, M. H. Huang, T. Li, S. Xu and F. X. Xiao, *J. Mater. Chem. A*, 2020, **8**, 177.
81 (*a*) X. Li, J. Yu, S. Wageh, A. A. Al-Ghamdi and J. Xie, *Small*, 2016, **12**, 6640–6696; (*b*) Q. Chen, J. L. Li, Q. L. Mo and F. X. Xiao, *Chem. Eng. J.*, 2024, **497**, 154584.
82 (*a*) K. I. Bolotin, K. J. Sikes, Z. Jiang, M. Klima, G. Fudenberg, J. Hone, P. Kim and H. L. Stormer, *Solid State Commun.*, 2008, **146**, 351–355; (*b*) X. Yan, B. X. Zheng, J. R. Zhu, Y. B. Li and F. X. Xiao, *Inorg. Chem.*, 2025, **64**, 3572–3581.
83 S. Gilje, S. Han, M. Wang, K. L. Wang and R. Kaner, *Nano Lett.*, 2007, **7**, 3394–3398.
84 Z. P. Zeng, F. X. Xiao, H. Phan, S. F. Chen, Z. Z. Yu, R. Wang, T. Q. Nguyen and T. T. Y. Tan, *J. Mater. Chem. A*, 2018, **6**, 1700–1713.
85 Z. Zeng, T. Li, Y. B. Li, X. C. Dai, M. H. Huang, Y. He, G. Xiao and F. X. Xiao, *J. Mater. Chem. A*, 2018, **6**, 24686.
86 P. Su, S. Li and F. X. Xiao, *Small*, 2024, **20**, 2400958.

87 L. X. Yin, G. Y. Xu, P. Nie, H. Dou and X. G. Zhang, *Chem. Eng. J.*, 2018, **352**, 695–703.
88 (*a*) X. J. Chen, X. D. Ren, Z. L. Liu, L. Zhuang and J. T. Lu, *Electrochem. Commun.*, 2013, **27**, 148–151; (*b*) Y. S. Cai, J. Q. Chen, P. Su, X. Yan, Q. Chen, Y. Wu and F. X. Xiao, *Chem. Sci.*, 2024, **15**, 13495–13505.
89 D. J. Yan, X. C. Fu, Z. C. Shang, J. K. Liu and H. A. Luo, *Chem. Eng. J.*, 2019, **361**, 853–861.
90 (*a*) Y. B. Li and F. X. Xiao, *J. Mater. Chem. A*, 2023, **11**, 589; (*b*) H. Liang, Q. Chen, Q. L. Mo, Y. Wu and F. X. Xiao, *J. Mater. Chem. A*, 2023, **11**, 9401–9426.
91 (*a*) Q. L. Mo, X. C. Dai, Y. Xiao and F. X. Xiao, *Chin. Chem. Lett.*, 2023, **34**, 107901; (*b*) B. X. Zheng, J. N. Yuan, P. Su, X. Yan, Q. Chen, M. Yuan and F. X. Xiao, *J. Mater. Chem. A*, 2025, **13**, 4908–4920.
92 Y. B. Li and F. X. Xiao, *Chem. Sci.*, 2025, **16**, 2661–2672.
93 (*a*) L. A. Peyser, A. E. Vinson, A. P. Bartko and R. M. Dickson, *Science*, 2001, **291**, 103–106; (*b*) X. Yan, M. Yuan, Y. L. Yuan, P. Su, Q. Chen and F. X. Xiao, *Chem. Sci.*, 2024, **15**, 10625–10637.
94 Y. S. Chen and P. V. Kamat, *J. Am. Chem. Soc.*, 2014, **136**, 6075.
95 Q. L. Mo, X. C. Dai and F. X. Xiao, *Small*, 2023, **19**, 2302372.
96 Y. Xiao, Q. L. Mo, G. Wu, K. Wang, X. Ge, S. R. Xu, J. L. Li, Y. Wu and F. X. Xiao, *J. Mater. Chem. A*, 2023, **11**, 2402.
97 P. Su, B. Tang and F. X. Xiao, *Small*, 2024, **20**, 2307619.
98 G. Li and R. Jin, *Acc. Chem. Res.*, 2013, **46**, 1749–1758.
99 M. S. Bootharaju, C. P. Joshi, M. R. Parida, O. F. Mohammed and O. M. Bakr, *Angew. Chem., Int. Ed.*, 2016, **55**, 922–926.
100 J. H. Zhou, W. C. Zhao, Z. H. Miao, J. G. Wang, Y. Ma, H. T. Wu, T. D. Sun, H. S. Qian and Z. B. Zha, *ACS Nano*, 2020, **14**, 2126–2136.
101 N. I. Gumerova and A. Rompel, *Nat. Rev. Chem.*, 2018, **2**, 0112.
102 K. V. Grzhegorzhevskii, P. S. Zelenovskiy, O. V. Koryakova and A. A. Ostroushko, *Inorg. Chim. Acta*, 2019, **489**, 287–300.
103 A. Ostroushko, I. Gette, I. Danilova, E. Mukhlynina, M. Tonkushina and K. Grzhegorzhevskii, *Nanotechnol. Russ.*, 2014, **9**, 577–582.
104 Y. Wu, X. X. Yu, Z. J. Fu, J. Y. Pei and L. H. Bi, *Catalysts*, 2021, **11**, 856.
105 J. Pei and L. Bi, *Catalysts*, 2022, **12**, 696.
106 Q. Zhou, Y. Du, Z. Y. Qu and L. H. Bi, *J. Electroanal. Chem.*, 2021, **894**, 115339.
107 D. Jeon, H. Kim, C. Lee, Y. Han, M. Gu, B. S. Kim and J. Ryu, *ACS Appl. Mater. Interfaces*, 2017, **9**, 40151–40161.
108 Y. Choi, D. Jeon, Y. Choi, D. Kim, N. Kim, M. Gu, S. Bae, T. Lee, H. W. Lee and B. S. Kim, *ACS Nano*, 2018, **13**, 467–475.
109 H. Kim, S. Bae, D. Jeon and J. Ryu, *Green Chem.*, 2018, **20**, 3732–3742.
110 L. Liu and A. Corma, *Chem. Rev.*, 2018, **118**, 4981–5079.
111 N. Zhang, C. Han, Y. J. Xu, J. J. Foley Iv, D. Zhang, J. Codrington, S. K. Gray and Y. G. Sun, *Nat. Photonics*, 2016, **10**, 473–482.
112 P. K. Ngumbi, S. W. Mugo and J. M. Ngaruiya, *IOSR J. Appl. Chem.*, 2018, **11**, 25–29.
113 L. Liu, X. Zhang, L. Yang, L. Ren, D. Wang and J. Ye, *Natl. Sci. Rev.*, 2017, **4**, 761–780.
114 Z. Cao, Y. L. Yin, P. Fu, D. Li, Y. L. Zhou, Z. J. Wen, Y. H. Peng, W. K. Wang, W. C. Zhou and D. S. Tang, *J. Electrochem. Soc.*, 2020, **167**, 026509.
115 F. X. Xiao, Z. P. Zeng and B. Liu, *J. Am. Chem. Soc.*, 2015, **137**, 10735–10744.
116 H. Kim, Y. You, D. Kang, D. Jeon, S. Bae, Y. Shin, J. Lee, J. Lee and J. Ryu, *Adv. Funct. Mater.*, 2019, **29**, 1906407.
117 M. Haase and H. Schäfer, *Angew. Chem., Int. Ed.*, 2011, **50**, 5808–5829.
118 (*a*) B. Zhou, B. Y. Shi, D. Y. Jin and X. G. Liu, *Nat. Nanotechnol.*, 2015, **10**, 924–936; (*b*) F. Wang, Y. Han, C. S. Lim, Y. H. Lu, J. Wang, J. Xu, H. Y. Chen, C. Zhang, M. H. Hong and X. G. Liu, *Nature*, 2010, **463**, 1061–1065.
119 Y. Lim, S. Y. Lee, D. Kim, M. Han, H. S. Han, S. H. Kang, J. K. Kim, U. Sim and Y. I. Park, *Chem. Eng. J.*, 2022, **438**, 135503.
120 F. X. Xiao, J. W. Miao and B. Liu, *J. Am. Chem. Soc.*, 2014, **136**, 1559–1569.
121 S. Bae, D. Kim, H. Kim, M. Gu, J. Ryu and B. S. Kim, *Adv. Funct. Mater.*, 2020, **30**, 1908492.
122 (*a*) M. Faraji, M. Yousefi, S. Yousefzadeh, M. Zirak, N. Naseri, T. H. Jeon, W. Choi and A. Z. Moshfegh, *Energy Environ. Sci.*, 2019, **12**, 59–95; (*b*) J. R. Zhu, Y. H. Chen, Z. Y. Li, Q. Chen and F. X. Xiao, *Inorg. Chem.*, 2023, **62**, 18649–18659.
123 M. Kavitha, P. Gopinath and H. John, *Phys. Chem. Chem. Phys.*, 2015, **17**, 14647–14655.
124 S. J. Teh, C. W. Lai and S. B. A. Hamid, *J. Energy Chem.*, 2016, **25**, 336–344.
125 D. Kim, M. Gu, Y. Choi, H. Kim, J. Ryu and B. S. Kim, *ACS Appl. Energy Mater.*, 2020, **3**, 7103–7112.
126 (*a*) P. T. Hammond, *Adv. Mater.*, 2004, **16**, 1271–1293; (*b*) X. Yan, J. H. Dong, J. Y. Zheng, Y. Wu and F. X. Xiao, *Chem. Sci.*, 2024, **15**, 2898–2913.
127 P. Bian, N. Li, G. Li, S. Zhang, X. Liu, J. Gu, B. Liu and T. Jiao, *Colloids Surf., A*, 2023, **656**, 130460.
128 J. L. Liu, X. Yan, J. N. Yuan, Y. Wu, X. Wang and F. X. Xiao, *Small*, 2024, **20**, 2405514.
129 J. N. Yuan, X. Yan, B. X. Zheng, J. Q. Chen and F. X. Xiao, *Inorg. Chem. Front.*, 2025, **12**, 1553–1567.
130 Z. Q. Wei and F. X. Xiao, *Inorg. Chem.*, 2023, **62**, 6138–6146.
131 Y. Yu, J. Y. Liu, S. S. Chen, Y. Song, R. R. Chen, J. Yu, J. H. Zhu, Y. Li, Q. Liu and J. Wang, *Chem. Eng. J.*, 2024, **486**, 149783.
132 B. Huang, G. F. von Rudorff and O. A. von Lilienfeld, *science*, 2023, **381**, 170–175.
133 A. Maqsood, C. Chen and T. J. Jacobsson, *Adv. Sci.*, 2024, **11**, 2401401.
134 X. P. Bai and X. C. Zhang, *Nano-Micro Lett.*, 2025, **17**, 135.
135 K. T. Butler, D. W. Davies, H. Cartwright, O. Isayev and A. Walsh, *Nature*, 2018, **559**, 547–555.